DTU Library

CFD investigation of flow in scour protection around a mono-pile with the volume-averaged k-ω model

Zhai, Yanyan; Christensen, Erik Damgaard

Published in:
Journal of Offshore Mechanics and Arctic Engineering

Link to article, DOI:
10.1115/1.4054393

Publication date:
2022

Document Version
Peer reviewed version

Journal of Offshore Mechanics and Arctic Engineering. Received February 21, 2022;
Accepted manuscript posted April 13, 2022. doi:10.1115/1.4054393

CFD investigation of flow in scour protection around a mono-pile with the volume-averaged *k-ω* model

Yanyan Zhai[a,]* and Erik Damgaard Christensen[a]

[a]Department of Mechanical Technology, Technical University of Denmark, DK-2800 Kgs. Lyngby, Denmark

*Corresponding author.

E-mail address: yzhai@mek.dtu.dk (Y. Zhai)

Abstract

The study numerically investigates the flow behaviour around a mono-pile with scour protection under steady and oscillatory flow conditions. A hydrodynamic model based on volume-averaged Reynolds-averaged Navier-Stokes (VARANS) equations with the volume-averaged *k-ω* turbulence closure is developed and implemented in OpenFOAM. Three porosity transition types, i.e., constant, linear and parabolic, near the interface between stone cover and free flow are firstly evaluated in two-dimensional models. The simulated results, i.e., flow velocities, turbulence levels and bed shear stresses, are compared to previous experiments under steady and oscillatory flow conditions. The parabolic transition shows the best agreement with the measurements and is therefore used in the developed model. Under steady current, a three-dimensional model is validated against experimental measurements including flow features both inside and outside of the scour protection around a mono-pile and it exhibits relatively good performance. Further, the volume-averaged *k-ω* model shows better agreement to experiments in porous medium compared to results from *k-ω* SST and volume-averaged *k-ε* models. The model is applied to investigate the flow patterns under oscillatory flow condition. The results show that a horseshoe vortex is formed and it penetrates the entire scour protection, which generates high flow velocities and bed shear stresses; erosion is most likely to occur at the area in the presence of vortex, which poses a threat to the pile stability. The simulations demonstrate the ability of the developed model to evaluate the flow behaviour in scour protection.

Keywords: monopile, scour protection, volume-averaged *k-ω* turbulence model, porous flow, OpenFOAM

1. Introduction

Offshore wind energy is developing rapidly as a principal source of renewable energy. Over the years, large quantities of offshore wind farms have been installed. For the stability of the structure, its foundation is a crucial component that still needs to be optimized. In the marine environment, the seabed in the vicinity of the foundation is often composed of sand or silt, where severe erosion occurs easily. Subjected to waves and currents, the increased hydrodynamic loads on the fine sediments result in local erosion around a pile foundation [1–3]. Without protection, the generated erosion would threaten the stability of the foundation.

Over the past few decades, a large number of studies are carried out to investigate the scour around the unprotected pile foundations through experiments and field studies. Most of the results have been compiled in Breusers and Raudkivi [4], Hoffmans and Verheij [5], Whitehouse [6], Melville and Coleman [7] and Sumer and Fredsøe [3].

Journal of Offshore Mechanics and Arctic Engineering. Received February 21, 2022;
Accepted manuscript posted April 13, 2022. doi:10.1115/1.4054393

They reveal that the surrounding seabed without protection suffers from erosion, and scour holes are thereby formed in some cases. To predict the evolution of scour holes, extensive numerical models have been established [8–17]. It is indicated that, with the elapse of time, the scour depth has a tendency of gradual increase. As a result, the scour would affect the stability of the foundation if countermeasures are not properly taken.

To protect the seabed from scouring, a submarine porous medium system, i.e., scour protection, as one practical approach is commonly designed and installed. The scour protection, composed of stone layers, is placed around the piles. The layers usually consist of both a filter layer and an armour layer. The latter ensures the stability of the piles under storm conditions, while the former prevents fine sediment from winnowing out of the scour protection through the large armour stones. In the presence of scour protections, the flow patterns and the sediment transport around the pile are altered, whereby the scouring issue is somehow alleviated. However, significant local sinking is observed during surveys of submarine scour protections in service [18–22]. Previous studies primarily investigate the sinking problem [23–26], in which the failure mode of scour protections is mostly predicted in an empirical way. Hansen et al. [18] also concluded that the sinking is induced by the removal of the base sediment. Through extensive physical model measurements, Nielsen et al. [27, 28] indicated that the horseshoe vortex is a key flow feature governing the sinking process of the scour protection, and it is also the essential element to cause erosion around unprotected piles [16, 29]. If the horseshoe vortex is strong enough to cause sediment transport in the scour protection, and as a result, the sinking of the scour protection occurs. The development of sinking increases free length of the monopile, which brings about the structural fatigue and damage. To figure out these processes, a detailed understanding of the flow inside the scour protections is thus necessary.

The flow behaviour inside the scour protections such as flow velocity, turbulence level and bed shear stress have been experimentally investigated [1, 27, 30, 31, 32]. Limitations do exist with numerical models to accurately describe these flow features. That is due to the fact that a complete resolution of the porous structure in scour protection is not yet feasible. To simulate porous flow, several resistance-type porosity models without turbulence model have been developed and applied without resolving the actual pores [33–36]. Later, Jensen et al. [37] derived volume-averaged flow equations to model the porous flow without using a turbulence closure, and the resistance force was added to account for the effect of the porous medium. A shortcoming is that the turbulent kinetic energy inside the porous media is not studied. These models assume that turbulence inside the porous media is negligible, and the assumption is only applicable when the permeability of the medium is comparatively small. However, in some cases the turbulent levels are of great importance [38, 39], and therefore, the turbulence closure is supposed to be taken into account.

To simulate turbulence in scour protection, some researchers used the LES model to closure the volume-averaged Reynolds-averaged Navier-Stokes equations (VARANS) [40–45]. However, the LES is time consuming and expensive computationally. Due to the limited computing resources, the standard turbulence models, e.g., k-ω, k-ω-SST and k-ε described in Wilcox [46], are typically applied. These closure models have to be modified in order to account for the porous media [37]. An example of the turbulent closure model for porous media is volume-averaged k-ε model [47]. However, the k-ε model is not suitable to simulate the adverse-pressure gradient flows [48, 49], which are induced by the interaction between the local hydrodynamics and the complex geometries of scour protection.

Journal of Offshore Mechanics and Arctic Engineering. Received February 21, 2022;
Accepted manuscript posted April 13, 2022. doi:10.1115/1.4054393

In this regard, we applied the volume-averaged method to the *k-ω* turbulence model [50], and validated the model against the experiments under steady current [51] and oscillatory flow [31, 51]. The computed results in the 2D cases are reasonably in line with the existing experiments and the model can accurately estimate the porous flow. However, in the presence of a monopile with scour protection, it is unclear whether the developed model is suitable for 3D cases due to the complex flow features, e.g., horseshoe vortex and lee-wake vortices. Moreover, a constant porosity of the porous medium is often assumed in existing numerical models for simplification, while it is not representative of real scenarios. In engineering practice, the porosity varies significantly near the interface between scour protection and free flow, but there are few studies analyzing the effect of porosity variations. These are the motivations of the present work, which will evaluate the porosity transition types near the interface, demonstrate the model performance and gives a detailed description of the flow pattern around a monopile with scour protection. For illustration, both steady and oscillatory flow conditions are taken into account.

The present paper is organized as follows. In Section 2, the numerical model is described briefly. The volume-averaged Reynolds-averaged Navier-Stokes equations (VARANS) developed by Jensen et al. [37] are rewritten and implemented as the governing equations. The volume-averaged *k-ω* equations, proposed by Zhai and Christensen [50], are employed as the closure. Section 3 analyses the effects of porosity transitions near the interface in 2D cases. In Section 4, the 3D model under steady current is validated against the existing experiments [27], and the results are also compared with those from the volume-averaged *k-ε* and the *k-ω* SST models. Application of the 3D model under oscillatory flow is subsequently presented and discussed in Section 5. Some main conclusions and remarks of the paper are finally given in Section 6.

2. Porous media model

2.1 Hydrodynamic equations

In the porous media model, the flow is governed by the volume-averaged continuity equation [52] and the VARANS equations [37]:

$$\frac{\partial \langle \bar{u}_i \rangle}{\partial x_i} = 0 \tag{1}$$

$$(1 + C_m)\frac{\partial}{\partial t}\frac{\rho\langle \bar{u}_i \rangle}{n} + \frac{1}{n}\frac{\partial}{\partial x_j}\frac{\rho\langle \bar{u}_i \rangle\langle \bar{u}_j \rangle}{n} + \frac{1}{n}\frac{\partial \rho\,\overline{\langle u_i' u_j' \rangle}}{\partial x_j} = -\frac{\partial \langle p \rangle^f}{\partial x_i} + g_j x_j \frac{\partial \rho}{\partial x_i} + \frac{1}{n}\frac{\partial}{\partial x_j}\mu\left(\frac{\partial \langle \bar{u}_i \rangle}{\partial x_j} + \frac{\partial \langle \bar{u}_j \rangle}{\partial x_i}\right) + F_i \tag{2}$$

For an oscillatory flow, the oscillating body force (B_i) is introduced into the Eq. (2) expressed as:

$$(1 + C_m)\frac{\partial}{\partial t}\frac{\langle \bar{u}_i \rangle}{n} + \frac{1}{n}\frac{\partial}{\partial x_j}\frac{\langle \bar{u}_i \rangle\langle \bar{u}_j \rangle}{n} + \frac{1}{n}\frac{\partial\,\overline{\langle u_i' u_j' \rangle}}{\partial x_j} = -\frac{1}{\rho}\frac{\partial \langle p \rangle^f}{\partial x_i} + g_j + \frac{1}{n}\frac{\partial}{\partial x_j}\nu\left(\frac{\partial \langle \bar{u}_i \rangle}{\partial x_j} + \frac{\partial \langle \bar{u}_j \rangle}{\partial x_i}\right) + \frac{F_i + B_i}{\rho} \tag{3}$$

where x_i = the Cartesian coordinates system, fluid density ρ = 1000 kg/m^3, F_i is introduced by volume-averaging process and consists of convective term, drag term and friction drag term, C_m = the inertial resistance force considering the transient effects of fluid accelerating around solid particles, t = time, n = the porosity, ν = the kinematic molecular viscosity, B_i = the body force, g_j = the acceleration of gravity, p = the pressure, $\bar{u}_i$= the mean component of the

Journal of Offshore Mechanics and Arctic Engineering. Received February 21, 2022;
Accepted manuscript posted April 13, 2022. doi:10.1115/1.4054393

velocity ($\bar{u}$, $\bar{v}$, $\bar{w}$). The fluctuating component of the velocity is u_i' and ‹› is the superficial volume averaging operator defined by:

$$\langle C \rangle = \frac{1}{V}\int_{V_f} C dV \tag{4}$$

where C is a scalar, vector, or tensor, V represents the total volume of solid and fluid phase and V_f is the volume of fluid phase.

The intrinsic average denoted by $‹›^f$ is defined as:

$$\langle C \rangle^f = \frac{1}{V_f}\int_{V_f} C dV \tag{5}$$

The relationship between these two averages is:

$$\langle C \rangle = n \langle C \rangle^f \tag{6}$$

where the n is given by:

$$n = \frac{V_f}{V} \tag{7}$$

According to the extended Darcy-Forchheimer relation, the C_m and the porous medium resistance force F_i are obtained. For C_m, the formulation proposed by van Gent [35] is adopted:

$$C_m = \gamma_p \frac{1-n}{n} \tag{8}$$

where γ_p = 0.34.

F_i is composed of the linear and non-linear resistance force, given by:

$$F_i = a\rho\langle \bar{u}_i \rangle + b\rho\sqrt{\langle \bar{u}_j \rangle \langle \bar{u}_j \rangle}\langle \bar{u}_i \rangle \tag{9}$$

where the a and b for oscillatory flow are expressed separately as:

$$a = \alpha \frac{(1-n)^2}{n^3}\frac{\nu}{D_{50}^2} \tag{10}$$

$$b = \beta(1 + \frac{7.5}{KC_s})\frac{1-n}{n^3}\frac{1}{D_{50}} \tag{11}$$

where α and β are empirical resistance parameters for resistance term, in this paper α = 500 and β = 2.0 [50], D_{50} = the median diameter of the porous medium, $KC_s = U_m T/(nD_{50})$ is the Keulegan-Carpenter number for stones, representing the ratio of the characteristic length scale of fluid particle motion to that of porous media [33, 37], in which, U_m = the maximum free stream velocity and T = the time period.

B_i is implemented to drive the flow and determined by differentiating the horizontal velocity. For oscillating flow, the periodic velocity is given by:

$$u(t) = U_m \sin(\omega_0 t) \tag{12}$$

where $\omega_0 = \frac{2\pi}{T}$. B_i is determined by:

$$B_i = \frac{du}{dt} = \omega_0 U_m \cos(\omega_0 t) \tag{13}$$

Journal of Offshore Mechanics and Arctic Engineering. Received February 21, 2022;
Accepted manuscript posted April 13, 2022. doi:10.1115/1.4054393

2.2 Volume-averaged k-ω equations

The VARANS equations are solved by utilizing the volume-averaged k-ω turbulence model as the closure. The turbulence closure model involves transport equations for the turbulent kinetic energy $\langle k\rangle$ and the specific dissipation rate $\langle\omega\rangle$ [50]:

$$\frac{\partial\langle k\rangle}{\partial t}+\frac{1}{n}\frac{\partial\langle k\rangle\langle\bar{u}_j\rangle}{\partial x_j}=\frac{\partial}{\partial x_j}\left[(\nu+\langle\nu_T\rangle\sigma^*)\frac{\partial\langle k\rangle}{\partial x_j}\right]-\frac{\langle\overline{u_i'u_j'}\rangle}{n}\frac{\partial\langle\bar{u}_i\rangle}{\partial x_j} -\frac{1}{n}\beta^*\langle\omega\rangle\langle k\rangle+n\beta^*\omega_\infty k_\infty \tag{14}$$

$$\frac{\partial\langle\omega\rangle}{\partial t}+\frac{1}{n}\frac{\partial\langle\omega\rangle\langle\bar{u}_j\rangle}{\partial x_j}=\frac{\partial}{\partial x_j}\left[(\nu+\langle\nu_T\rangle\sigma)\frac{\partial\langle\omega\rangle}{\partial x_j}\right]-\frac{1}{n}\frac{\gamma\langle\omega\rangle}{\langle k\rangle}\langle\overline{u_i'u_j'}\rangle\frac{\partial\langle\bar{u}_i\rangle}{\partial x_j} -\frac{1}{n}\beta_1\langle\omega\rangle^2+n\beta_1\omega_\infty{}^2 \tag{15}$$

where the superficial averaged eddy viscosity read:

$$\langle\nu_T\rangle=\gamma^*\frac{\langle k\rangle}{n\langle\omega\rangle} \tag{16}$$

where $\gamma^*=1$. The model constants, k_∞ and ω_∞, are defined separately by:

$$k_\infty=0.85\frac{(1-n)}{\sqrt{n}}\left(\langle\bar{u}_j\rangle^2\right) \tag{17}$$

$$\omega_\infty=117\frac{(1-n)^{1.5}}{D_{50}\sqrt{n}}\left(\langle\bar{u}_j\rangle^2\right)^{1/2} \tag{18}$$

and the closure coefficients are: γ = 0.52, σ^*= 0.5, β^*= 0.09, σ = 0.5 and β_1 = 0.075. For a detailed description of the process, see our recent paper [50].

3. Analysis of porosity transition near the interface

The scour protection is usually modelled as a homogeneous medium with constant properties in the entire porous zone, which does not in a realistic way accommodate variations near the interface between free flow and porous medium. To illustrate the variations, Fig. 1 shows a sketch of a realistic interface with multi-layer stones. Near the interface, the porosity, n, is not a constant and we can assume a transition from the value in porous zones to 1 in free flow. Let h_s = the height of the stone cover. Larger ratio of D_{50}/h_s increases the transition effect. For a single layer with large stones, D_{50}/h_s = 1 the concept of porosity loses its meaning as it is intended for a medium with individual solids smaller than the scale of the entire medium.

To illustrate the effect of the porosity variation near the interface, we analyse three transition types, i.e., constant, linear variation and parabolic variation. The transition height h_v is associated with the geometry of stones and is described as a linear relation with D_{50}, $h_v = \lambda D_{50}$. For stone cover with one, two and three layers, the λ was determined empirically by Stevanato et al. [31] according to the measured velocity profiles inside stone cover. Assuming that the porosity variation follows the velocity variation, then λ = 0.45 for a single layer of stones and λ = 1.05 for two and three layers.

Journal of Offshore Mechanics and Arctic Engineering. Received February 21, 2022;
Accepted manuscript posted April 13, 2022. doi:10.1115/1.4054393

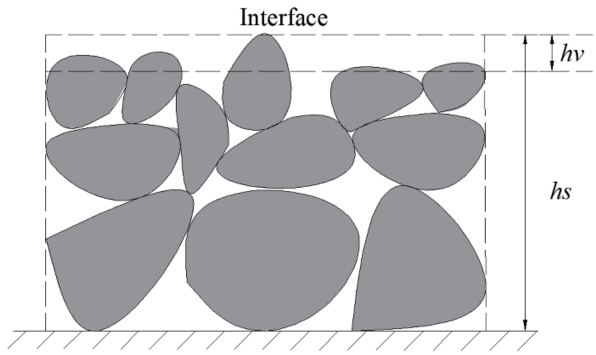

Fig. 1 Sketch of a realistic interface between porous medium and free flow.

Data from previous experimental studies are used to determine the variation of porosity, *n*, near the interface. Sumer et al. [1] and Stevanato et al. [31] conducted flow experiments over stone covers under steady and oscillatory flow conditions. The measured results in terms of velocity profile, bed shear stress and turbulent kinetic energy are utilized for the analysis of the porosity transition type.

3.1 Steady current

Under steady state, the experiments of Sumer et al. [1] were carried out in a flume with cyclical water supply. Fig. 2 sketches the experimental layout in terms of geometry and dimensions. Its length, width and height were 28.0, 0.6 and 0.8 m. A 9.2 m long and 0.09 m high false bottom was placed on the flume bottom as the working section, to get a complete side view for flow visualization. The false bottom was covered by stones (D_{50} = 38.5 mm and *n* = 0.4). In the working section, the water depth was 0.4 m. The Laser Doppler Anemometer (LDA) was used to measure velocity at five cross-sections, and the mean flow velocity *U* (averaged over water depth) = 38.7 cm/s. The parameter of friction velocity U_f = 5.22 cm/s based on the logarithmic profile of the flow above the stones. More detailed information is given by Sumer et al. [1] and Fredsøe et al. [53].

Our numerical model in 2D is set up to match the experiment. The computational domain is resolved with 65,709 non-uniform computational cells to ensure that the distance y_c^+ from the wall-adjacent cell centers to the wall is about 30. The computational mesh is automatically constructed by the snappyHexMesh tool. Grid convergence is made through three sets of mesh (coarse, medium and fine) with reference to the velocity, and the medium mesh (65,709 cells) is shown to be the optimum. The boundary conditions are defined at the inlet, outlet and walls. For velocity, a uniform *U* = 33 cm/s is specified at the inlet resulting in a mean velocity of *U* = 38.7 cm/s at the working section. A zero normal gradient condition ($\frac{\partial u}{\partial x} = 0$) is used at the outlet; a slip boundary condition is imposed at the top wall to model the flow with free surface and a non-slip condition is specified at the bottom wall. In regards to pressure, zero pressure is specified at both inlet and outlet; a zero pressure gradient is given at the top and bottom walls. At the inlet, $k = 1.36 \times 10^{-4}$ m^2/s^2 and $\omega = 0.16$ s^{-1}, which are based on the turbulent intensity of 5% of the inlet velocity, with a length scale of 20% of the channel width; at the outlet, *k* and *ω* are both specified with a zero gradient condition. The timestep is set as 0.0001 s and the total simulation time is 1000 s, which is found to provide a stationary solution. The selected timestep is determined by calculating the Courant number (preferably ≤ 0.4), so that the

Journal of Offshore Mechanics and Arctic Engineering. Received February 21, 2022;
Accepted manuscript posted April 13, 2022. doi:10.1115/1.4054393

information propagation of the physical flow is captured. About 15.2 m of the inlet, the simulated results are extracted for comparison with the measured data.

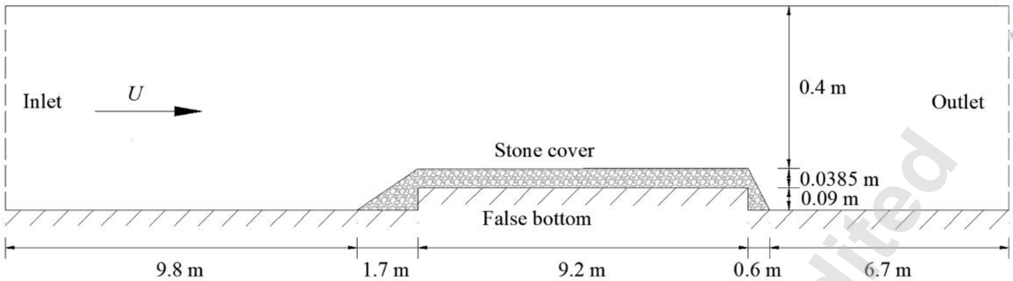

Fig. 2 Sketch of the experimental layout for steady current through a porous medium.

To illustrate the effect of the porosity transition on the velocity distribution, the simulated velocity profiles with three different transitions and the measured velocities are depicted in Fig.3. All computed velocity profiles follow a similar pattern and are in line with the measured results outside the porous media. With a constant porosity, the velocities inside the porous medium tend to be underestimated, while in the free flow they are slightly overestimated. Compared to measured values, the velocity profile from the linear porosity exhibits some slight deviations, but still better than the results with the constant porosity.

Turbulence is essential for sediment transport in the porous medium, and turbulent kinetic energy k is the crucial parameter to estimate the turbulence level. In the porous medium, the k is related to turbulence fluctuation U_s by $U_s = \sqrt{0.6k}$ according to Zhai and Christensen [50]. The ratio between the turbulent fluctuation and the friction velocity, U_s/U_f, is compared to experimental results in Fig. 4. In the vertical direction, the profiles in simulated U_s/U_f for all porosity transitions are similar to the measured one. U_s/U_f increases from the free flow towards the to the porous medium and peaks closely to the interface. From the interface it decreases further down into the media. In the porous medium, the U_s/U_f profiles from parabolic and linear porosity transitions show good agreement with measurements, while the profile for constant porosity presents obvious deviations from the measurements. In the outer flow, the computed U_s/U_f results with the parabolic transition match well with the measured data, while the results for the linear transition and constant porosity have appreciable deviations. Therefore, for steady current, the numerical model provides better velocity and turbulence calculations when the parabolic transition in the porosity zone is implemented.

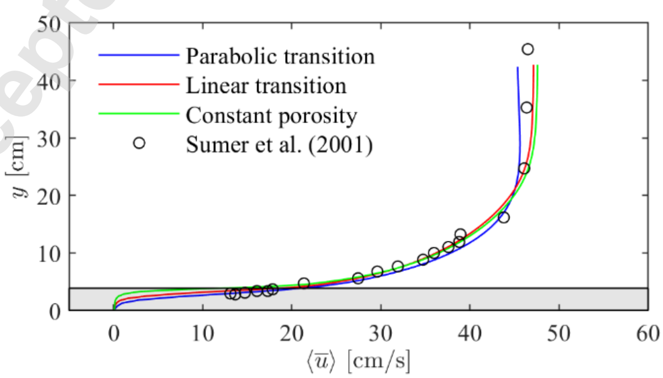

Fig. 3 Comparisons of simulated and measured velocity profiles.

Journal of Offshore Mechanics and Arctic Engineering. Received February 21, 2022;
Accepted manuscript posted April 13, 2022. doi:10.1115/1.4054393

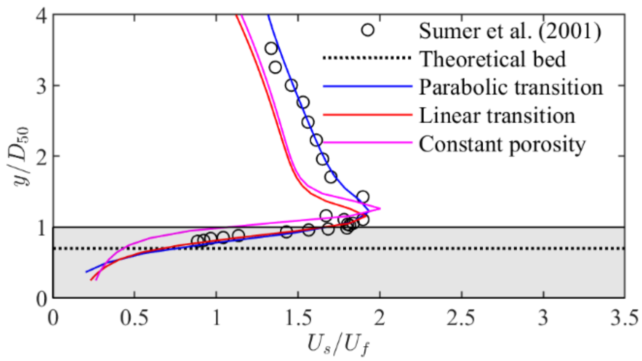

Fig. 4 Comparisons of simulated and measured turbulent kinetic energy.

3.2 Oscillatory flow

Under oscillatory flow condition, Stevanato et al. [31] carried out the flow experiments over stone covers. The measured results that included velocity profile, bed shear stress and turbulent kinetic energy are utilized for the analysis of the porosity transition type.

The experiments were performed in an oscillatory U-tube device with risers installed at the tube's both ends to generate the oscillatory flow. The horizontal rectangular working section was 15.8 m long, 0.39 m wide and 0.29 m high. Stones were placed on the bottom to form a 8.6 m long and 0.108 m high stone cover. The median stone diameter was, D_{50} = 36 mm, and the porosity n = 0.4. The maximum free stream velocity was, U_m = 0.96 m/s with a period of T = 9.73 s. Based on the expression given in Section 2.1, the KC_s = 648.67.

LDA was used to measure the flow velocities. The velocities above the stones were measured at the centreline of the tube to reduce effects of secondary flows. To avoid the laser beams being blocked by stones, the velocities in the pores were measured nearby the sidewall. A Dantec hot-film probe measured the bed shear stress beneath the stone layer. Further details are given in Stevanato et al. [31] and Sumer et al. [54].

The numerical model reproduces the experiment with the same geometry of the horizontal working section. Fig. 5 shows the sketch of the numerical setup. The model in 2D domain is resolved by 56,588 non-uniform computational cells. For the velocity, the applied oscillatory body force is imposed over the domain after an iterative process to reach the experimental U_m; a no-slip boundary is specified at the walls and a zero gradient at the inlet and outlet. For the turbulent quantities, zero gradients are specified at the inlet and outlet; the wall functions are used at the walls. For pressure, we use zero gradients at walls; the cyclic boundary conditions at the inlet and outlet based on the analysis of pressure boundary conditions in Schippers et al. [55]. To achieve stable results, the time step is 0.0001 s and the total simulation time is set to 350 s. The results in the period 291.9 s < t < 301.6 s are selected for analysis according to Zhai and Christensen [50].

Under the oscillatory flow conditions, the influence of porosity transition on the velocity distribution is analysed. Fig. 6 shows the velocity profiles at four different phases ($\omega_0 t = 45^\circ, 90^\circ, 135^\circ$ and 180°). In the lower layer ($y \leqslant 7$ cm), the profiles from the three porosity transitions are almost straight lines and coincide with each other at each phase, which implies that the velocities are almost constant. The computed profiles, irrespective of any transition type, fit well with the measured ones, especially at the phase of 45°, 90° and 135°. In the upper layer (y > 7

Journal of Offshore Mechanics and Arctic Engineering. Received February 21, 2022;
Accepted manuscript posted April 13, 2022. doi:10.1115/1.4054393

cm), the velocity profile with the parabolic transition shows a better agreement with measured results for all four phases. The model with the linear transition apparently under-predicts the velocity although it gives a similar profile to the measurements. At all four phases, the velocity profiles with the constant porosity deviate from the experimental results. In the case of the constant porosity, the velocity decreases quickly from the free flow to the top of the porous medium, which is mainly attributed to the sharp porosity transition. In addition, the velocity at the interface with constant porosity is about 70% smaller than that with the parabolic transition.

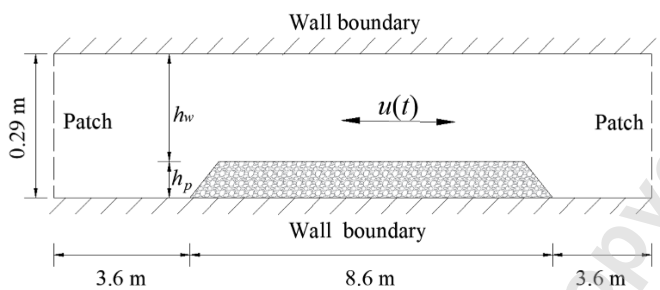

Fig. 5 Sketch of the numerical model setup for oscillatory flow through a porous medium.

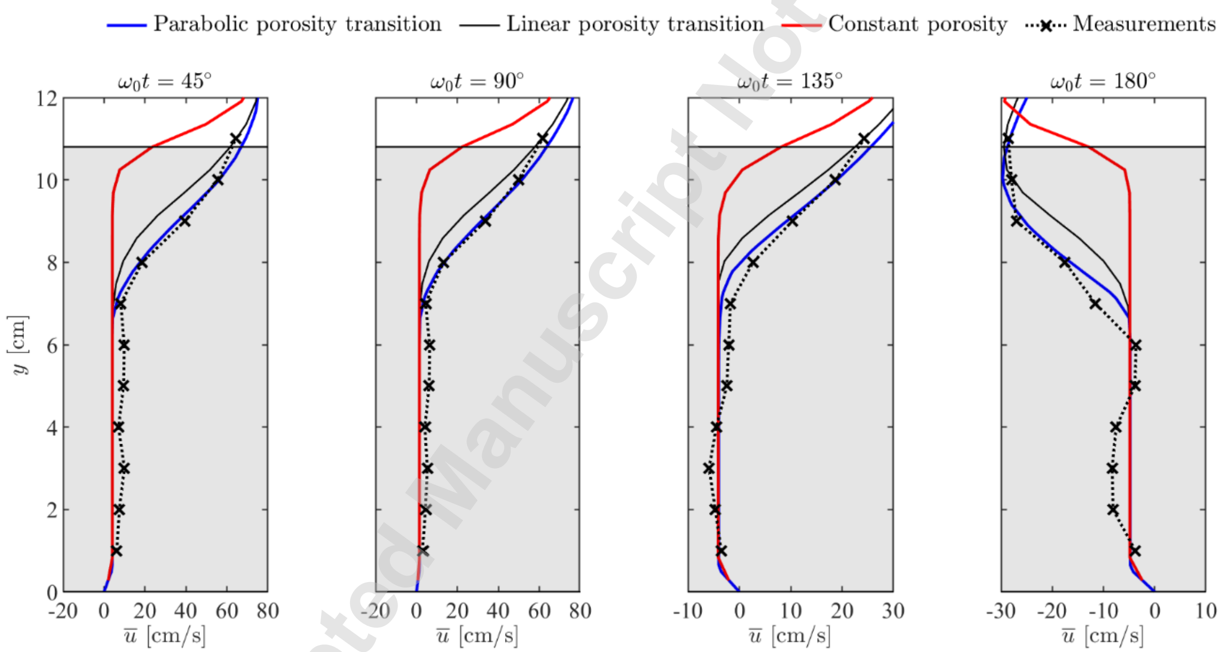

Fig. 6 Comparisons of velocity profiles with different porosity transitions near the interface.

At the interface, the turbulent kinetic energy is mainly induced by the velocity gradients. To illustrate the effect of porosity transition on turbulent level, the numerical and experimental results of U_s over the depth at the same four phases are depicted for comparison in Fig. 7. The experimental results show the U_s varies noticeably from the interface to y = 7 cm, implying that the turbulence dissipates in a swift manner, which is also confirmed by the simulations.

Journal of Offshore Mechanics and Arctic Engineering. Received February 21, 2022;
Accepted manuscript posted April 13, 2022. doi:10.1115/1.4054393

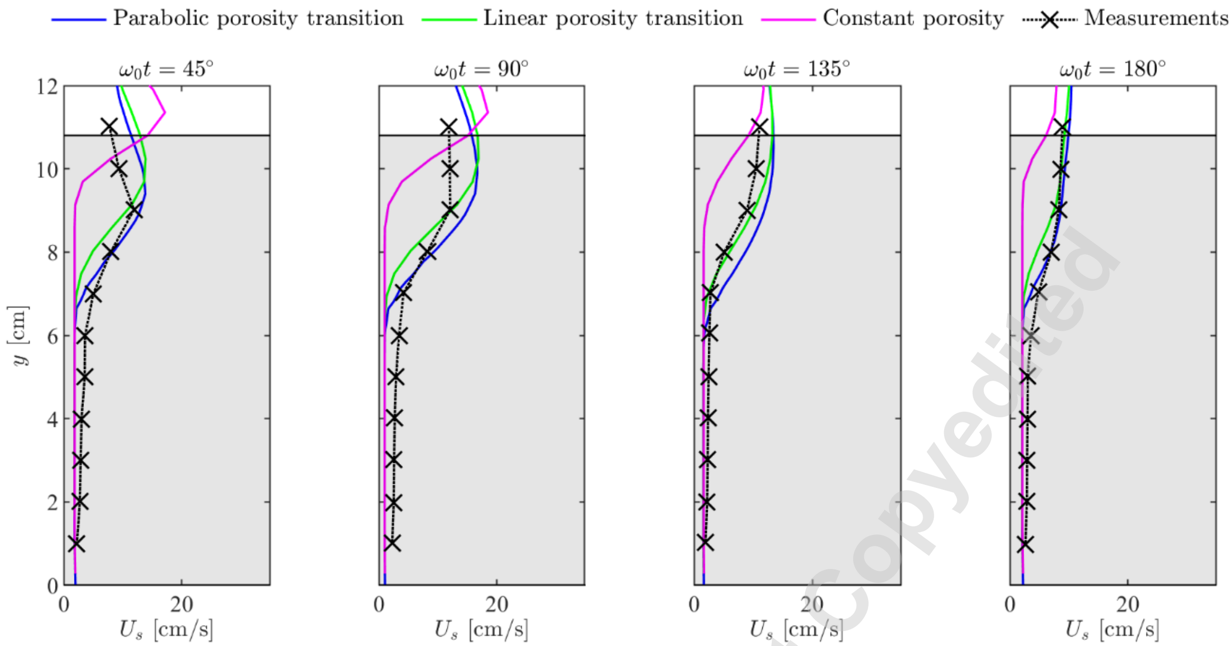

Fig. 7 Comparisons of turbulent fluctuations with different porosity transitions near the interface.

For $y \leqslant 7$ cm, the simulated U_s are roughly in a line with the experimental results, which illustrates the porosity transition type has probably no effect on the turbulence variation in the deeper part. For $y > 7$ cm, the simulations with parabolic and linear transitions show similar U_s profiles with measurements, although the magnitude differs by and large. The U_s is overestimated under the two transition types, and the former seems to be better especially at the interface in terms of 45°and 90°. However, with the constant porosity, the U_s is underestimated for 7 cm < $y \leqslant 10$ cm and is overestimated for $y > 10$ cm, presenting a significant deviation from the measured profile. It is also noted that in the deeper part, it has relatively small velocities and thereby producing less turbulence. Near the interface, the porosity transitions affect the flow resistance and result in the larger velocity gradients, which generate large turbulence dispassion.

As the porosity transition changes from constant to linear to parabolic, the peak position of U_s gradually moves downward (Fig. 7) at the four phases. For instance, with $\omega_0 t = 45°$, the maximum locates at $y \approx 11$ cm for the constant porosity and at $y \approx 9$ cm for the parabolic transition. A similar change is also observed in the places where the constant velocity occurs (Fig. 6), for example, $y \approx 10$ cm for the constant porosity and $y \approx 7$ cm for the parabolic transition at $\omega_0 t = 45°$. This is related to the increased porosity in the upper layer during this process. It indicates that the greater the porosity, the deeper the turbulent flow penetrates into the porous medium.

To further illustrate the effect of porosity transitions on flow, the induced bed shear stress τ_b, as a basis for describing the sediment transport, is analyzed. Fig. 8 shows the comparison of the simulated and measured τ_b. In the experiment, the τ_b was measured in three different layouts of the stones. Pore 1 and 2 were measured at the center of a pore, and in the case of pore 3 there was a streamwise offset in the measured location. It presents that the τ_b calculated with the three porosity transitions is in the right order of magnitude with measurements and is well represented over all phases of a time period. The model produces similar τ_b profiles irrespective of any transition type

Journal of Offshore Mechanics and Arctic Engineering. Received February 21, 2022;
Accepted manuscript posted April 13, 2022. doi:10.1115/1.4054393

considered, and the difference is minor. This is explained by the fact that the τ_b is associated with the velocity gradients and turbulence level, at the bed they are unaffected by the porosity transitions, as illustrated in Figs. 6 and 7.

Based on these analyses, the model with parabolic transition considered shows better agreement to the measurements in terms of porous flow velocity, bed shear stress and turbulence levels. Therefore, the parabolic transition near the interface is adopted in Section 4.

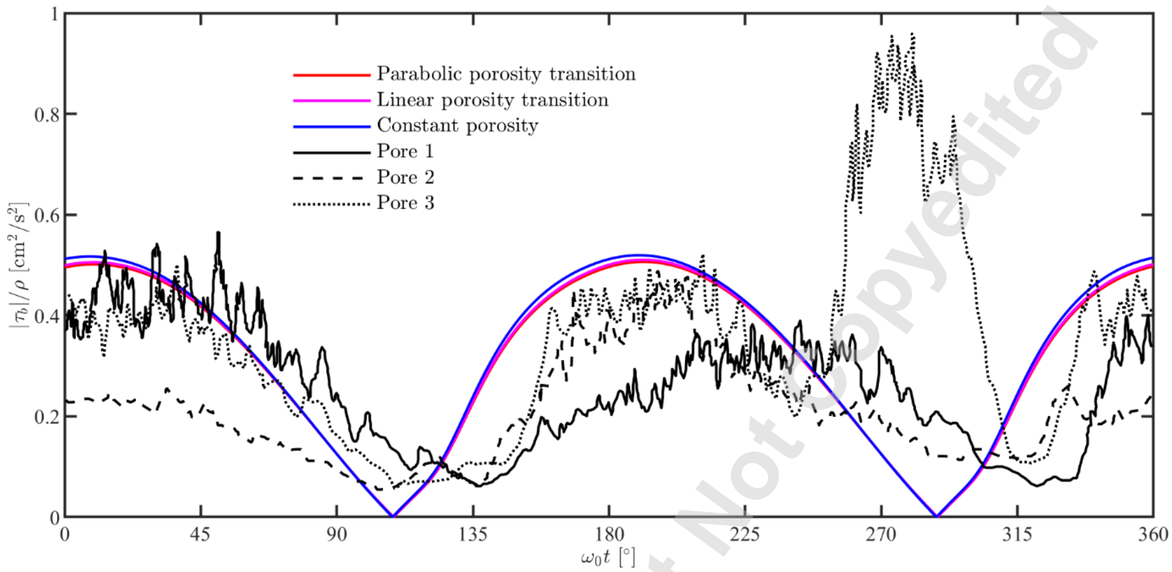

Fig. 8 Comparisons of bed shear stresses with different porosity transitions near the interface.

4. Validation of the model under steady current

To validate the proposed volume-averaged k-ω turbulence model in the presence of a mono-pile, a 3D model is set up under a steady current. The parabolic porosity variation is applied near the interface between the free flow and the porous media. The calculated velocity profile and turbulence level are compared to experiments conducted by Nielsen [27].

The experiments were conducted in a flume with recirculation pump to provide a steady flow. Fig. 9 shows a sketch of the experimental layout. The flume was 23.0 m long, 2.0 m wide and 0.5 m high. About 15.0 m downstream of the inlet, a false bottom (white plastic plate) was installed in the wave tank. Its length, width and height were 3.05 m, 2.0 m and 5.0 mm, respectively. The plate had a 15.0 cm long taper on the upstream end with a slope of 1:6. A pile with a diameter of 14.0 cm was placed on the plate, whose centre point was approximately 0.9 m to the plate downstream end and 1.0 m to the sidewall. The scour protection with a diameter of 78.0 cm was placed around the pile and consisted of one layer of irregular crushed stones. The median diameter of the crushed stones was D_{50} = 4.3 cm and the porosity n = 0.4. The water depth was 0.50 m and the incoming U = 0.40 m/s. To measure the velocity, the submerged pen-size LDA probe was adopted. More details are available in Nielsen et al. [28, 30].

Journal of Offshore Mechanics and Arctic Engineering. Received February 21, 2022;
Accepted manuscript posted April 13, 2022. doi:10.1115/1.4054393

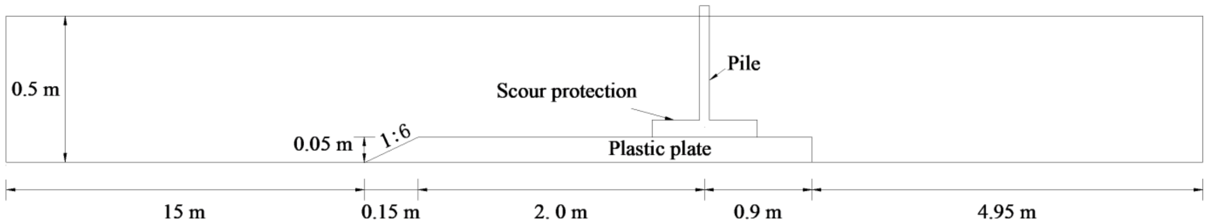

Fig. 9 A schematic layout of the experiment.

The numerical model has the same dimensions as the experiment with respect to the flume width and height, while the length is shortened to 12.0 m to save computational resources. The shortening is made mainly on the seaside of the structure. Fig. 10 shows a sketch of the model domain and boundary type. The pile and the scour protection with the same dimensions as the experiment, are placed about 7.0 m downstream of the inlet. In view of the size of the pile and scour protection, the up-and downstream distances are sufficient to remove any dependency of the boundaries in the results.

In order to analyse the grid dependence on the numerical solutions, three different discretizations have been adopted including a fine grid with 2,334,778 cells, a medium grid with 1,254,508 cells and a coarse grid with 702,576 cells. The computational mesh is constructed using snappyHexMesh generator. The results show that the force on the pile obtained for the first two grids is almost identical, except for very small scale details. Therefore, in order to save computational resources, the model domain is resolved with a total of 1,254,508 non-uniform cells, see Fig 11. These cells are distributed over 16 computational cores on a high performance cluster. The grid refines toward the bottom and the pile surface, where the wall-adjacent cell thickness is 0.0036 m and 0.0018 m.

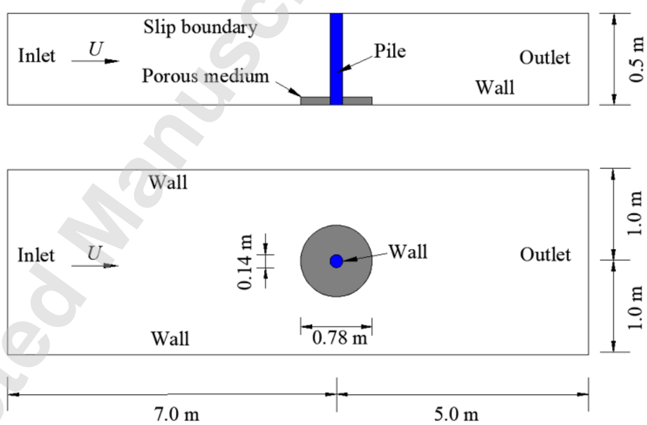

Fig. 10 Sketch of the numerical model domain and boundary definitions.

Journal of Offshore Mechanics and Arctic Engineering. Received February 21, 2022;
Accepted manuscript posted April 13, 2022. doi:10.1115/1.4054393

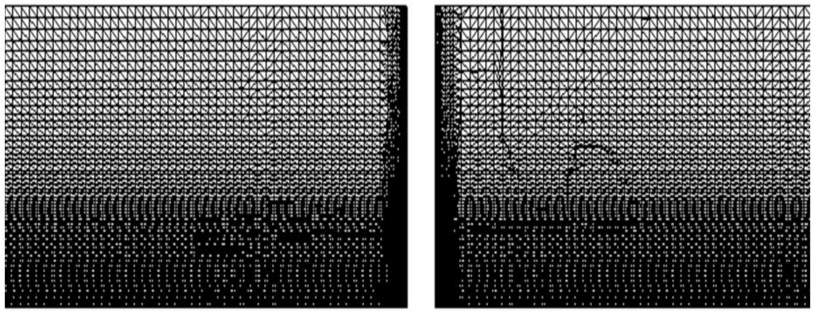

(a)

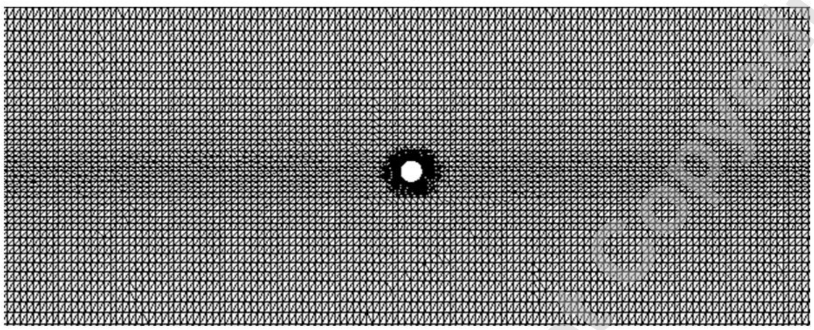

(b)

Fig. 11 Computational mesh with pile: (a) side view and (b) bird view.

The boundary conditions are defined at the inlet, outlet and walls including the pile surface. A uniform velocity of U = 0.40 m/s is specified at the inlet, and the zero normal gradient condition is used at the outlet; a slip boundary condition is imposed at the top wall to model the flow with free surface and a non-slip condition is specified at the bottom wall as well as the pile surface. In regards to pressure, a zero pressure gradient is given at both inlet and outlet, and the top, bottom and sides' walls. At the inlet, $k = 2\times10^{-4}$ m^2/s^2 and $\omega = 0.258$ s^{-1}; at the outlet, k and ω are both specified with a zero gradient condition. At the walls, the wall functions for k and ω are used. To obtain a stationary solution, the time step is 0.0001 s and the total simulation time is 1000 s.

To compare the simulated velocity profiles with the measurements, Fig. 12 shows the profiles at six cross-sections upstream of the pile. The Figs. 12a, b correspond to the measured results and the simulated ones with the volume-averaged k-ω model, respectively. In general it shows a good agreement between model results and measured velocity profiles by Nielsen [27], although their magnitudes differ in a minor way inside the scour protection. An apparent return flow in the porous medium is observed up to about 10.0 cm from the edge of the pile, which is consistent with the flow measurements. In addition, the return flow exhibits a first increase and then decrease pattern, which is also visualized in the experiments. It is also noted that, in the range of -28.0 cm $< x < -7.0$ cm below $z = 3.5$ cm, the measured velocities (Fig. 12a) are slightly larger than the simulated ones (Fig. 12b). This implies that the present model does not prevent the horseshoe vortex in penetrating into the stone cover. The flow pattern upstream of the pile also coincides with that observed by, for example, Roulund et al. [16] and Graf and Yulistiyanto [56] for an unprotected pile.

The upstream directed flow near the bottom is generated by the horseshoe vortex that penetrates into the porous medium. The comparison in the Figs. 12a, b indicates that the vortex is predicted well by the numerical model.

Journal of Offshore Mechanics and Arctic Engineering. Received February 21, 2022;
Accepted manuscript posted April 13, 2022. doi:10.1115/1.4054393

In the present case, the horizontal size of the horseshoe vortex is approximately 13.0 cm, as shown in Fig. 12b, and it is a little smaller than the pile diameter (14.0 cm). That is because the size and strength of the vortex are determined by both pile diameter and flow velocity [27]. The horseshoe vortex is almost completely embedded in the porous medium due to the relatively thin protection layers. According to Roulund et al. [16], the vortex is believed to generate high bed shear stresses that cause sediment transport. This can also be illustrated by the high flow velocities near the bottom beneath the stone cover (Fig. 12). The vortex penetrating into the porous medium transports the sediment adjacent to the pile upstream. If it is strong enough, the scoured particles will be winnowed by the main flow and transported downstream, causing the sinking of scour protection. Otherwise, these particles will deposit in between the stones.

The results from the volume-averaged k-ε model are also included for illustration (Fig. 12c). In comparison to the measurements (Fig. 12a), the numerical model also reproduces the similar flow patterns around the pile, especially outside the porous medium. However, inside the porous medium, the flow magnitudes differ appreciably although the horizontal flow directions are identical. For example, the simulated velocities at $x = -20$ cm are larger than the measured ones, and the opposite is the case for the other cross-sections. It indicates that the simulated horseshoe vortex in size is comparatively larger than the measured one, while its intensity is relatively smaller. By comparing the results from the two volume-averaged models (Fig. 12b, c), they both reasonably capture the flow features, while regarding the return flow inside the porous medium, the volume-averaged k-ω model gives a better picture with reference to the measurements.

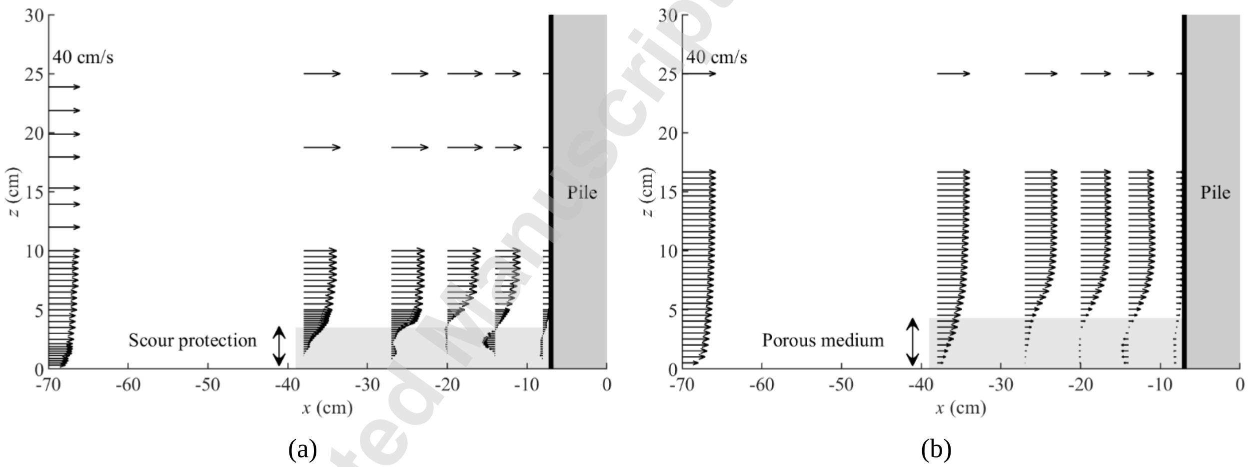

Journal of Offshore Mechanics and Arctic Engineering. Received February 21, 2022;
Accepted manuscript posted April 13, 2022. doi:10.1115/1.4054393

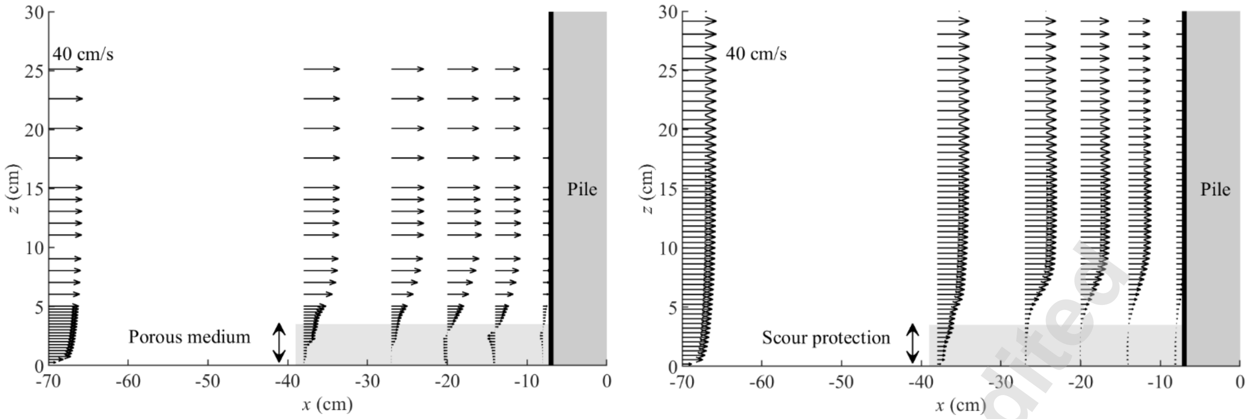

(c) (d)

Fig. 12 Velocity profiles at six cross-sections upstream of the pile: (a) measurements, adapted from Nielsen et al. [28]; (b) simulations with the volume-averaged *k-ω* model; (c) simulations with the volume-averaged *k-ε* model; (d) simulations with the *k-ω* SST model.

Moreover, one more simulation is carried out in which the *k-ω* SST model is considered, and the velocity profiles are shown in Fig.12d. The results show a much weaker return flow from the horseshoe vortex than the measurements (Fig.12a) and the results with both volume-averaged models (Fig.12b, c). Without using the volume-averaged procedures in the porous medium, too much resistance would be introduced for the horseshoe vortex, leading to a smaller vortex in size and intensity. This further illustrates the improvement of the volume-averaged *k-ω* model in the prediction of the horseshoe vortex.

To further elaborate the flow features around the pile, Fig. 13 shows the horizontal and vertical velocity fields corresponding to $\bar{u}$ and $\bar{w}$ from the volume-averaged *k-ω* model. In Fig. 13a, positive values denote the streamwise flow and negative ones return flow. In Fig. 13b, positive values denote the upflow and negative ones downflow. The Fig. 13a presents that the return flow occurs both in the scour protection and immediately downstream the pile. The former is a result of horseshoe vortex penetration from the free flow to the protection layer; the latter is attributed to the lee-wake vortices. The simulated downstream $\bar{u}$ is in general lower than the upstream one, and the $\bar{u}$ in the scour protection is also relatively small compared to that in the outer flow. The overall flow patterns are almost consistent with the patterns observed by Nielsen et al. [28].

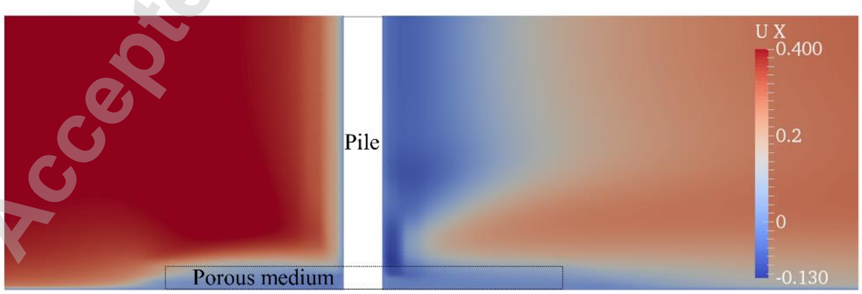

(a)

Journal of Offshore Mechanics and Arctic Engineering. Received February 21, 2022;
Accepted manuscript posted April 13, 2022. doi:10.1115/1.4054393

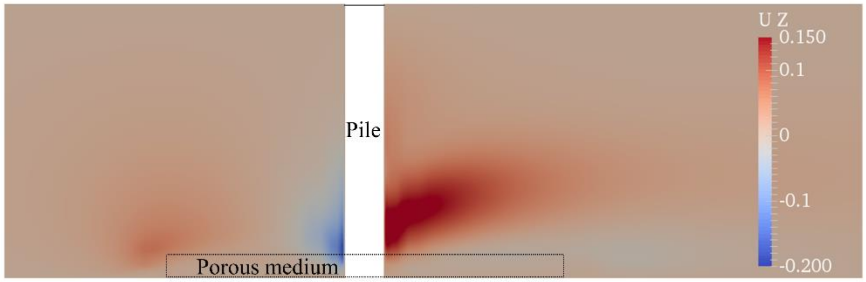

(b)

Fig. 13 Velocity fields around the mono-pile with scour protection: (a) $\bar{u}$-component in m/s, (b) $\bar{w}$-component in m/s.

In Fig. 13b, it appears that there is an obvious downflow in front of the pile, while it only exists on the top of the scour protection. The reason is the porous resistance quickly dampens the downflow into the scour protection. The downflow is driven by the deceleration of the flow, and it adds to the rotation of the horseshoe vortex. The upflow is observed behind the pile and it becomes weak gradually along the streamwise direction, which is in relation to the development of the lee-wake vortices.

In addition to the velocity profile, the k as the other essential quantity associated with sediment transport, is also presented for analysis. Sumer et al. [57] pointed out that the sediment transport is augmented by a factor of 6 when the k near the bottom ascends by 20%. Together with the measured k, Fig. 14 plots the simulated k profiles at the same six cross-sections upstream of the pile. In the figure, the black dots represent the measured values, the red and blue lines refer to the simulated results with the volume-averaged k-ω and k-ε models, respectively. The black lines denote the simulated results with the k-ω SST model. It illustrates that the numerical results with the two volume-averaged turbulence models exhibit similar profiles and follow the distribution of the measured values. The k reaches a peak roughly near the interface and it declines gradually towards the free flow and the bottom. However, the k-ω SST model significantly overestimates the k values near the interface; the peak positions move upward and deviate from the measurements, especially at $x = -14.0$ and -8.0 cm. This suggests that both volume-averaged models produce reasonable turbulence levels in comparison with the measurements.

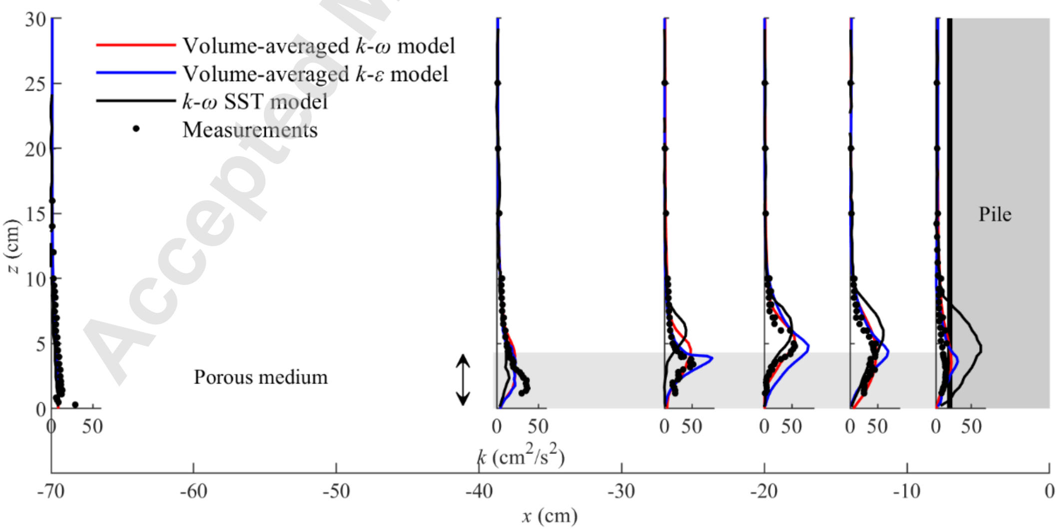

Journal of Offshore Mechanics and Arctic Engineering. Received February 21, 2022;
Accepted manuscript posted April 13, 2022. doi:10.1115/1.4054393

Fig. 14 Turbulent kinetic energy profiles at six cross-sections upstream of the pile. The black dots represent the measured values; the red and blue lines refer to the simulated results with the volume-averaged *k*-*ω* and *k*-*ε* models, respectively; black lines denote the simulated results with the *k*-*ω* SST model.

At the undisturbed flow area, e.g., $x = -70.0$ cm, the simulated results from both models agree with the measurements. As the incoming flow comes close to the medium, the turbulent kinetic energy, k, is slightly underestimated. This is understandable as the model mainly induces turbulence at the interface with the free flow owing to the flow shearing. The induced turbulence is transported downwards from the interface to the bottom, as the flow moves along the streamwise direction. At the upstream end of the porous medium, i.e., $x = -38.0$ cm, the flow is not very sheared and as a result, and less turbulence is generated compared to the measurements. When the flow approaches the pile, e.g., at $x = -27.0$ cm, -20.0 cm, -14.0 cm and -8.0 cm, the simulated k from the volume-averaged *k*-*ε* model is significantly over predicted, especially near the interface. While, the result from the volume-averaged *k*-*ω* model is generally in the right order of magnitude compared to the measurement, apart from minor local overestimation at $x = -27.0$ cm and -8.0 cm. This implies that the latter could evaluate the turbulence levels more accurately than the former. It is also observed that the k has relatively large values upstream of the pile, e.g., between $x = -20.0$ and -14.0 cm, which is likely coupled with the fact that the flow at this locations is subjected to the horseshoe vortex. These are also confirmed by Zhai and Christensen [50] with 2D validation cases involving a scour protection.

It appears that no previous experimental results are available with respect to the τ_b in the surrounding of the pile. However, the τ_b is a key parameter that is closely associated with sediment transport. The distribution of τ_b from the numerical model is presented in Fig. 15a. The enlargement view presenting the τ_b in the scour protection is shown in Fig. 15b. In the figure, it is visualized by contours of τ_b magnitude. The white circular area at the center is the mono-pile and the dashed circle is the porous medium. As expected, the τ_b reduces considerably inside the porous medium, and also in the separation zones in front of and in the lee-wake side of the porous medium. Additionally, it shows that there is a concentration of bed shear stress between the front and the side edges of the pile. This is due to the strong presence of the horseshoe vortex.

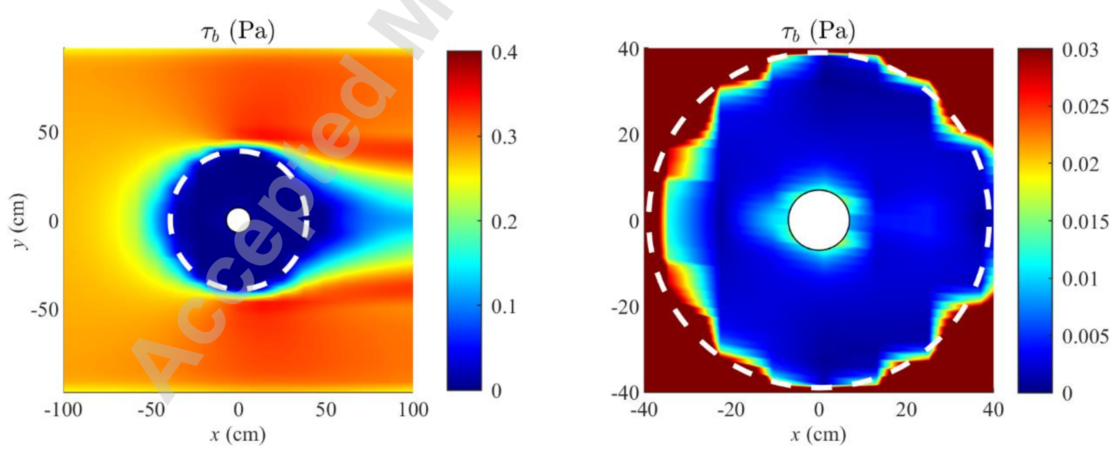

(a) (b)

Fig. 15 Simulated bed shear stress: (a) in the surrounding of the pile; (b) the enlargement view.

Journal of Offshore Mechanics and Arctic Engineering. Received February 21, 2022;
Accepted manuscript posted April 13, 2022. doi:10.1115/1.4054393

Taking the Figs. 12–15 into account, the velocities, turbulence levels and bed shear stresses upstream of the pile are relatively high due to the penetration of horseshoe vortex into the protection layer. To conclude, the volume-averaged *k*-*ω* model has a relatively good performance for studying the flow around a pile both inside and outside of the scour protection.

5. 3D model application under oscillatory flow

After validation of the model under steady state, it is used to investigate the flow around a full-scale pile with scour protection under oscillatory flow. The schematic layout of the numerical setup is shown in Fig. 16. The model domain is 20 m long, 20 m wide and 6 m high. The pile is placed centrally in the domain and its diameter, D_p, is 3 m. The scour protection with three stone layers is modelled in the shape of a truncated conical section; its bottom diameter is 11 m and top diameter 8.6 m. The median stone diameter is, D_{50} = 0.40 m and the porosity is, n = 0.4. Similar to Section 4, three discretizations, i.e., 2,000,000 cells, 2,259,600 cells and 3,390,400 cells, are considered to analyse the grid convergence in terms of the force on the pile. The force obtained for the last two grids is almost identical, except for very small scale details. Therefore, in order to save computational resources, the computational domain is resolved with 2,259,600 non-uniform cells, see Fig. 17. These cells are distributed over 24 computational cores on a high performance cluster. The grid refines toward the bottom and the pile surface where the wall-adjacent cell thickness is 0.0050 m and 0.0015 m.

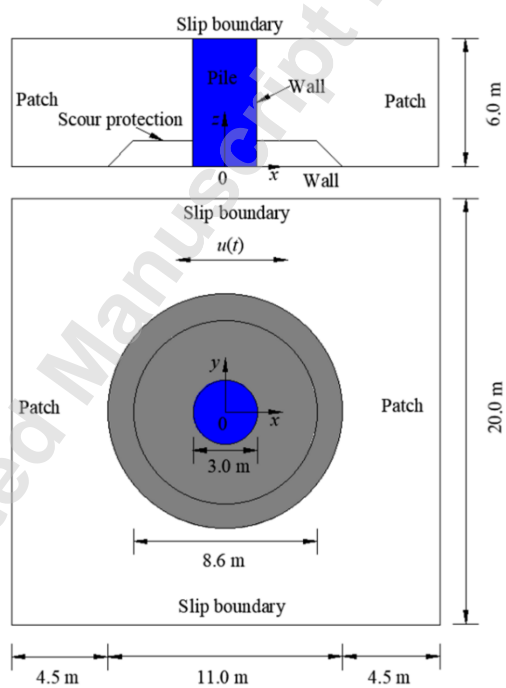

Fig. 16 Schematic layout of the numerical setup and boundary definitions.

Journal of Offshore Mechanics and Arctic Engineering. Received February 21, 2022;
Accepted manuscript posted April 13, 2022. doi:10.1115/1.4054393

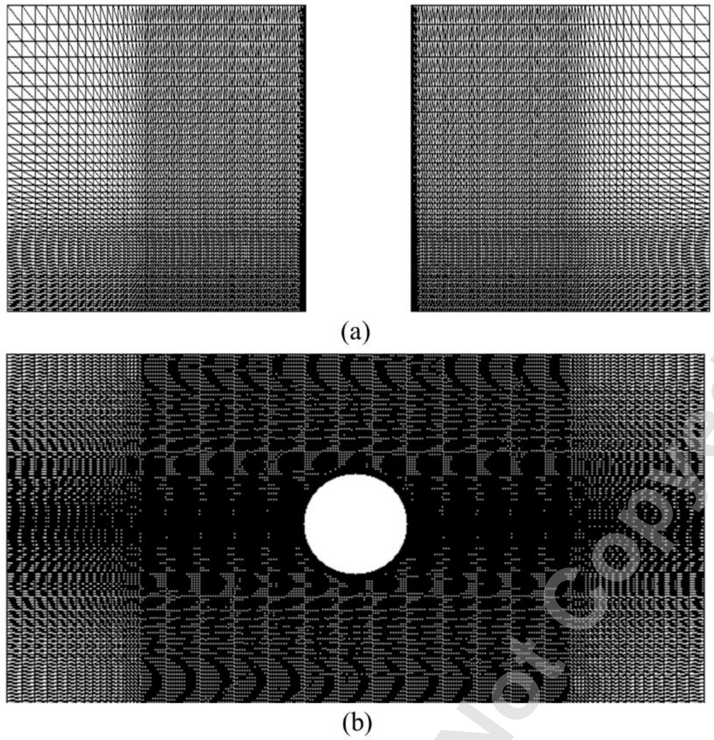

Fig. 17 Computational mesh with pile: (a) side view and (b) bird view.

Same boundary conditions are defined at the inlet, outlet and walls as the ones in the 3D steady state model, while for the oscillatory flow, two kinds of flows with the same period T = 12 s, are studied. One is the U_m = 1.50 m/s and the other is U_m = 1.95 m/s. The corresponding KC_s values are 112.50 and 146.25, respectively. The boundary definitions are also illustrated in Fig. 16. At the inlet, $k = 1.36 \times 10^{-4}$ m^2/s^2 and ω = 0.16 s^{-1}; at the outlet, k and ω are both specified with a zero gradient condition. When the pile is placed in oscillatory flow, the Keulegan-Carpenter number for pile, KC_p, has to be introduced. It defines the oscillatory motion related to the diameter of the pile, D_p, which is calculated with $KC_p = U_m T / D_p$. Based on the given flow conditions and mono-pile diameter, the KC_p = 6.0 and 7.8, respectively, which meet the critical limit (KC_p = 6.0) for the formation of a horseshoe vortex in the front of a pile without scour protection [58]. To achieve stable results, the time step is 0.0001 s and the total simulation time is 500 s.

For the two flow cases, the undisturbed flows are sampled after they reach stability. Fig. 18 depicts the time series of the outer flow velocity, sampled at $x = -10.0$ m and z = 5.0 m in the plane of symmetry y = 0. It shows that the signal follows a sinusoidal variation for the two cases. The symmetry in the oscillatory flows causes the symmetry of flow features between the crest and trough half-periods, thereby the results of the crest half-period are selected for analysis.

Journal of Offshore Mechanics and Arctic Engineering. Received February 21, 2022;
Accepted manuscript posted April 13, 2022. doi:10.1115/1.4054393

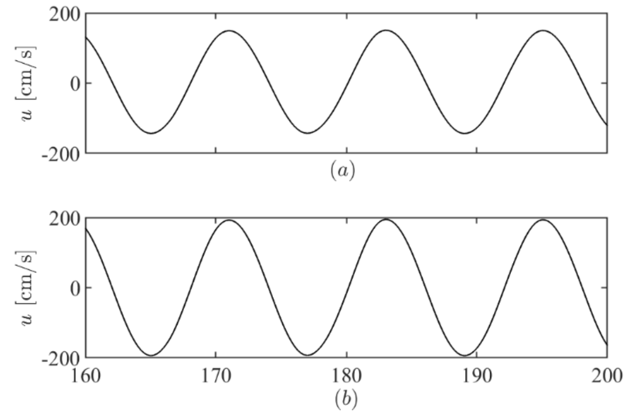

Fig. 18. Time series of the undisturbed free-stream velocity with T = 12 s. (a) U_m = 1.50 m/s; (b) U_m = 1.95 m/s.

To examine the periodical flow patterns (U_m = 1.50 m/s and T = 12 s), eight phases, i.e., $\omega_0 t$ = 45°, 75°, 90°, 105°, 120°, 135°, $150^\circ$and 165° in a crest half-period ($0^\circ - 180^\circ$) are selected for illustration, as presented in Fig. 19. The water flows from left to right. On the left side of the pile a horseshoe vortex emerges for phases at $\omega_0 t$ = 105°, 120°, 135°, 150° and 165°. This is almost in line with the predictions that the vortex is expected to appear in the phase interval 110° < $\omega_0 t$ < 170° without scour protection [3]. The size and strength of the vortex grows as the flow develops (105° < $\omega_0 t$ < 165°). As the vortex strengthens inside the porous medium the return flow in terms of range and size also increases. In front of the pile, we see that the near-bed flow velocity at the right hand side of the porous medium edge first declines (45° < $\omega_0 t$ < 135°) and then increases (150° < $\omega_0 t$ < 165°) in the reverse direction. After $\omega_0 t$ reaches about 165°, the vortex breaks down and washed out prior to the flow reversal ($\omega_0 t = 180^\circ$), and eventually disappear.

Journal of Offshore Mechanics and Arctic Engineering. Received February 21, 2022;
Accepted manuscript posted April 13, 2022. doi:10.1115/1.4054393

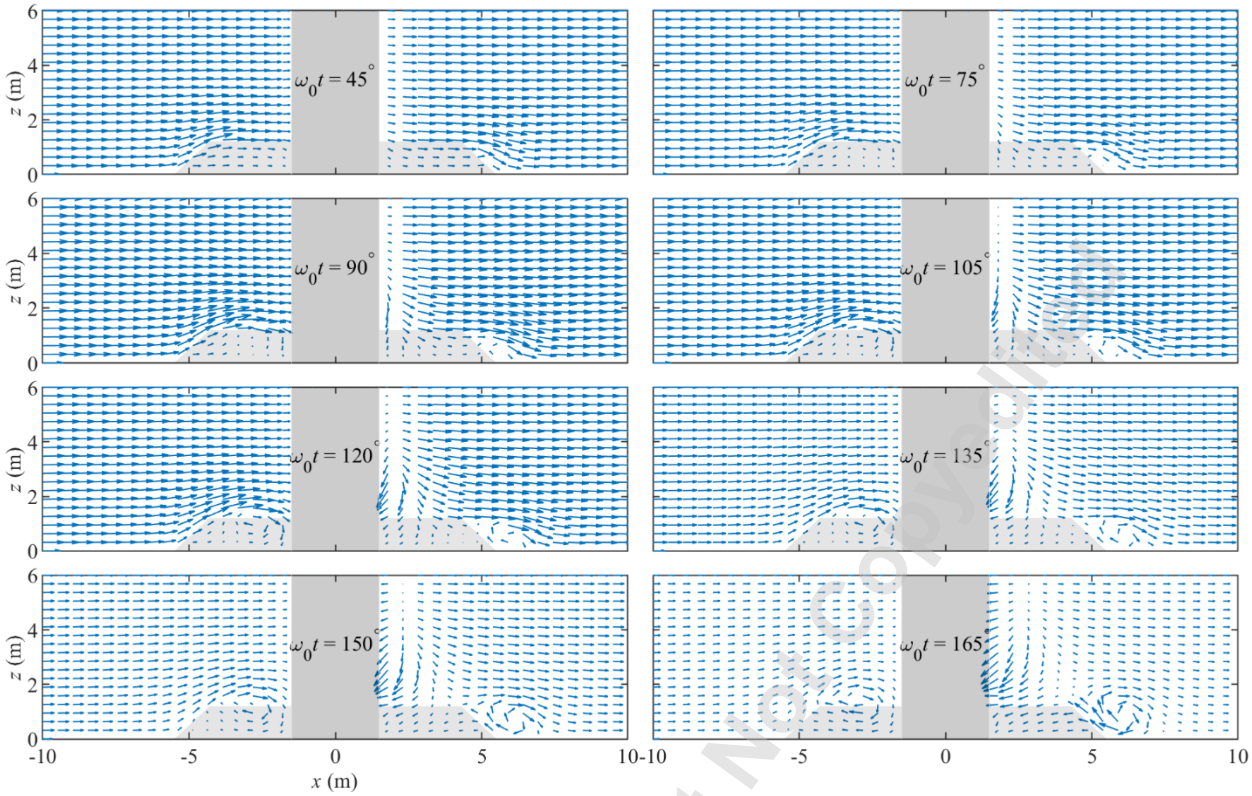

Fig. 19 Velocity fields around the pile with scour protection at different phases for the crest half-period (U_m = 1.50 m/s, T = 12 s and KC_p = 6.0).

No wave and combined wave-current measurements are made around a pile within the scour protection. Therefore, we draw an analogy to flow around a pile without scour protection [58], where we expect the horseshoe vortex in the case of waves to be small. In such a case, the size and strength of the horseshoe vortex are determined by both flow velocity and pile size. The vortex system is in a form of one dominating vortex, i.e., single horseshoe vortex system. The reason is that the thickness of scour protection is smaller than the pile diameter, otherwise, two clockwise rotating vortices might appear in the vicinity of the pile, which is revealed through experiments by Nielsen et al. [28]. Similarly to the steady current in Section 4, the vortex penetrates into the entire scour protection. The down-flow adjacent to the pile decreases from the interface to the bottom due to the porous resistance, and only a small amount continues up and out from the porous medium.

Immediately behind the pile, there occurs reverse flow with the increased phase, implying the occurrence of lee-wake vortex. Compared to the horseshoe vortex, the attached lee-wake vortex near the porous medium first emerges earlier at $\omega_0 t = 90^\circ$, while it in the free flow first appears later at $\omega_0 t = 120^\circ$. Similar to the horseshoe vortex, the lee wake vortex grows in size and intensity gradually after its generation ($\omega_0 t < 165^\circ$), which can be observed from the increased reverse velocity behind the pile (Fig. 19). This results in that as $\omega_0 t$ increases from 75° to 165°, the near-bed wake vortex penetrates deeper into the porous medium. Fig. 19 shows that the near-bed velocity first decreases (45° < $\omega_0 t$ < 105°), and then increases inversely (105° < $\omega_0 t$ < 165°) behind the pile. At the downstream

Journal of Offshore Mechanics and Arctic Engineering. Received February 21, 2022;
Accepted manuscript posted April 13, 2022. doi:10.1115/1.4054393

edge of the scour protection, a distinct vortex rotating in clockwise direction occurs at $\omega_0 t$ = 105°, 135°, 150°and 165°.

Corresponding to the same phases, the bed shear stress field, τ_b, around the pile and scour protection is analyzed, as shown in Fig. 20a. The τ_b distribution in the domain is symmetric with reference to y = 0. Outside the porous medium, the bed shear stress, τ_b is relatively large compared with bed shear stress in inside. The τ_b shows an increase from $\omega_0 t$ = 45° to 90°, followed with a decrease from $\omega_0 t$ = 90° to 165°. This is consistent with the variation of flow velocity during the first half-period. The flow runs from left to right, and it is noted that behind the porous medium, the location of τ_b with minor values moves along the streamwise direction at a certain distance. Adjacent to the scour protection on the right side, the area with enhanced τ_b appears at $\omega_0 t$ = 105° and it amplifies obviously with the increasing $\omega_0 t$ from 105° to 165°, which coincides with development of vortices observed in Fig. 19.

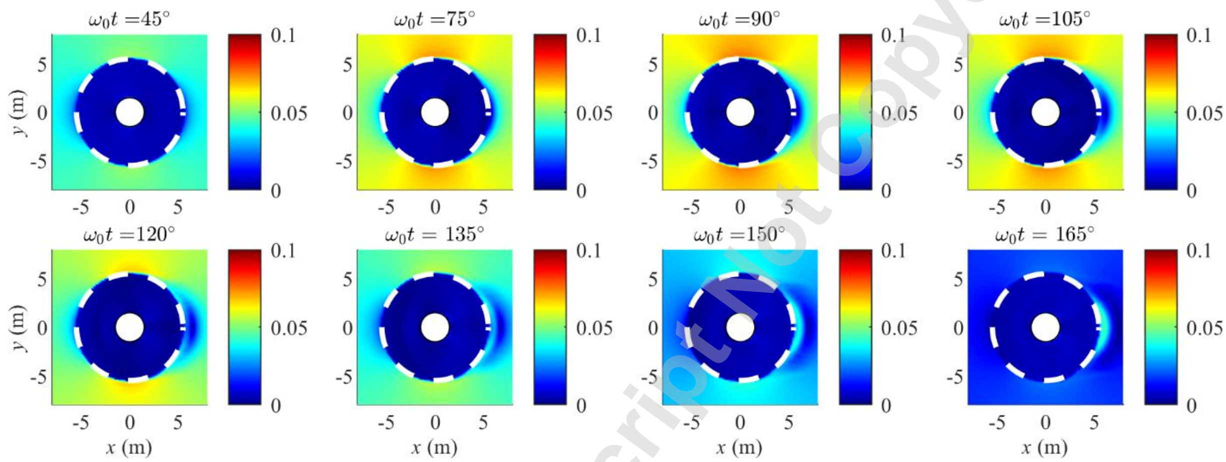

(a)

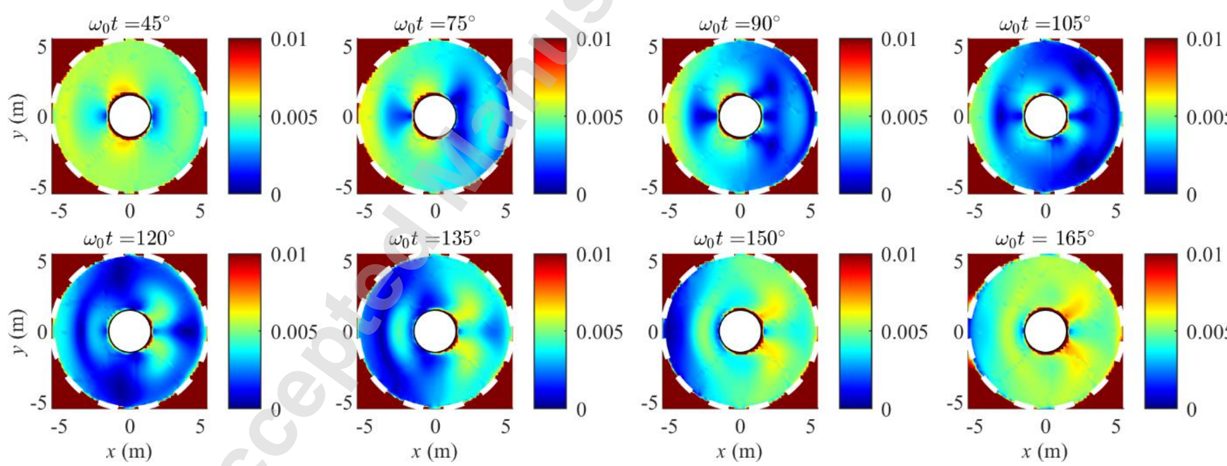

(b)

Fig. 20 Bed shear stress around the pile with scour protection at different phases for the crest half-period (U_m = 1.50 m/s, T = 12 s and KC_p = 6.0): (a) in the whole domain and (b) enlargement view inside the porous medium.

Inside the porous medium, the enlargement view of the bed shear stress, τ_b, distribution is presented in Fig. 20b. From $\omega_0 t$ = 45° to 90°, the area directly in front of the pile features a small τ_b and its range expands

Journal of Offshore Mechanics and Arctic Engineering. Received February 21, 2022;
Accepted manuscript posted April 13, 2022. doi:10.1115/1.4054393

symmetrically with reference to $y = 0$. A similar phenomenon is also observed at the lee-wake side of the pile. We observe high bed shear stresses, τ_b, between the front and the side edges of the pile, and its amplification at the lee-wake side of the pile is small. This distribution is similar to the experimental enhanced τ_b values with a symmetrical distribution to the sides, which is attributed to the changes in size and intensity of the horseshoe vortex. At both sides downstream of the pile, the τ_b shows a symmetric distribution and its values increases significantly ($90^\circ < \omega_0 t < 165^\circ$). This also illustrates that, behind the pile, a pair of symmetric attached vortices are formed.

Exposed to oscillatory flows, the flow features around a pile with scour protection is primarily related to the KC_p, and in influence on generation of the horseshoe vortex. To further understand the effect of KC_p on the flow patterns, Fig. 21 presents a sequence of panels illustrating the development of the velocity fields during approximately one half-period of the oscillatory flow for $KC_p = 7.8$. It shows that, in front of the pile, a horseshoe vortex exists at $\omega_0 t = 90^\circ$ and it is not formed at $\omega_0 t = 75^\circ$, which is inferred that the vortex begins to emerge between 75° and 90°. Once the vortex has emerged, it becomes enhanced with the increased phase (e.g., from 90° to 165°) and eventually disrupted and washed just prior to the reversed flow at $\omega_0 t = 180^\circ$. Without the scour protection, Sumer et al. [58] predicted that the vortex appears in the phase interval $90^\circ < \omega_0 t < 170^\circ$ for $KC_p = 7.8$. The vortex appears at a slightly earlier phase in the case with scour protection, which obviously leads to larger lifespans. The reason is that, in front of the pile, the flow velocity is increased due to the presence of the scour protection and large adverse pressure gradient is generated at an earlier phase.

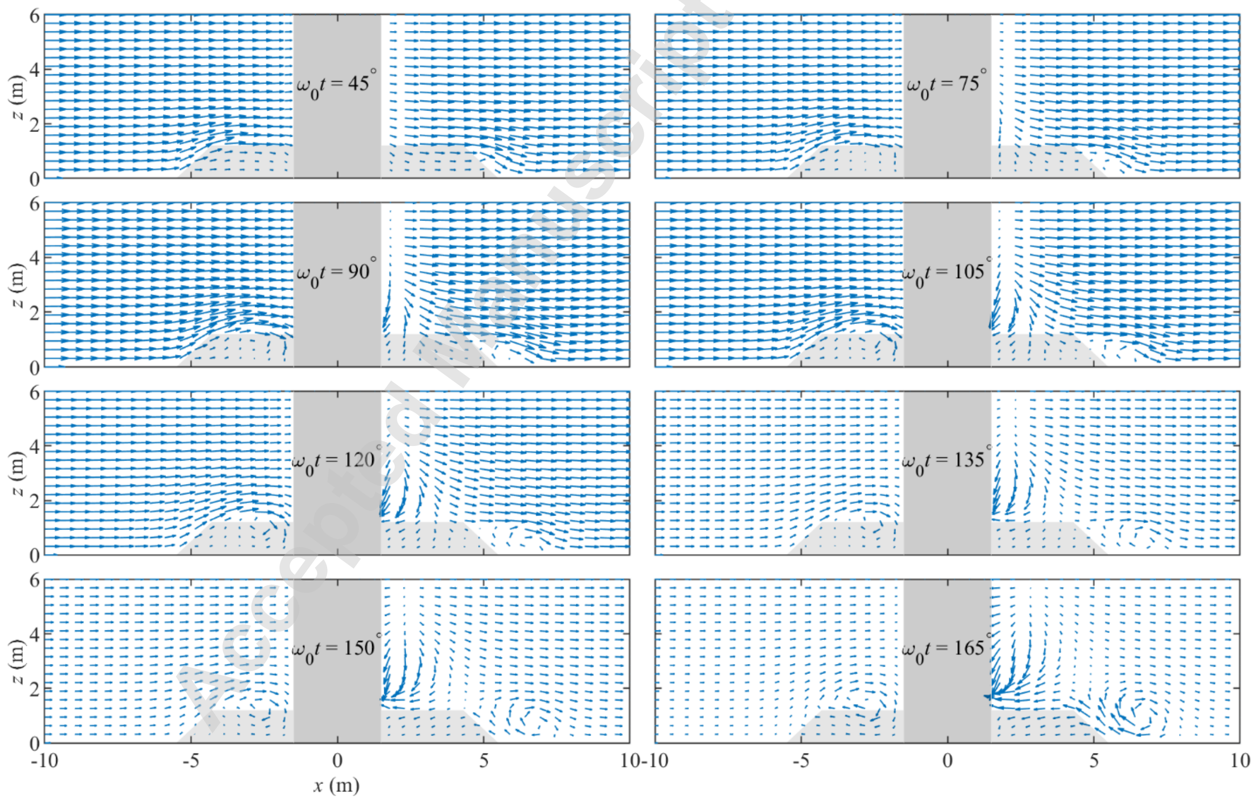

Fig. 21 Velocity fields around the pile with scour protection at different phases for the crest half-period ($U_m = 1.95$ m/s, $T = 12$ s and $KC_p = 7.8$).

Journal of Offshore Mechanics and Arctic Engineering. Received February 21, 2022;
Accepted manuscript posted April 13, 2022. doi:10.1115/1.4054393

The lee-wake vortex near the porous medium occurs first at $\omega_0 t$ = 75° and it in the free flow emerges first at $\omega_0 t$ = 105°. Besides, at the downstream edge of the scour protection, a clockwise vortex emerges in the interval of $\omega_0 t$ = 90° – 165°, and it grows in size with the phase. The vortices shift their locations in each half-period, and the horseshoe vortex in front of the pile is supposed to be symmetric to that at the back of the pile, due to the symmetric oscillatory flow. Compared to the case where KC_p = 6.0, the vortices inclusive of the horseshoe vortex, the lee-wake vortices and the clockwise vortex all emerge earlier, and are maintained over a larger span of $\omega_0 t$. Similarly, their size and intensity also increases with increasing $\omega_0 t$. This illustrates the variations of the vortices as the KC_p increases from 6.0 to 7.8. These findings are in line with Sumer and Fredsøe [3], who made visualization of horseshoe vortex in front of a pile without scour protection, and found the horseshoe vortex to increase in both size and lifespan as the KC_p increases.

To further illustrate the effect of KC_p variations on the flow features, during the course of the same crest half-period ($0^\circ - 180^\circ$), the τ_b for KC_p = 7.8 around the pile and scour protection are analyzed, as shown in Fig. 22a. The close-up of its distribution inside the porous medium is presented in Fig. 22b. Similar to the τ_b distributions for KC_p = 6.0, symmetry of the τ_b distribution, with reference to *y* = 0, is also observed under all phases for KC_p = 7.8. In the front of and in the lee-wake side of the pile, the τ_b amplifies symmetrically with the development of the vortices. The τ_b is significantly influenced by the KC_p, increasing the KC_p from 6.0 to 7.8, its value becomes large, which is expected according to the flow fields.

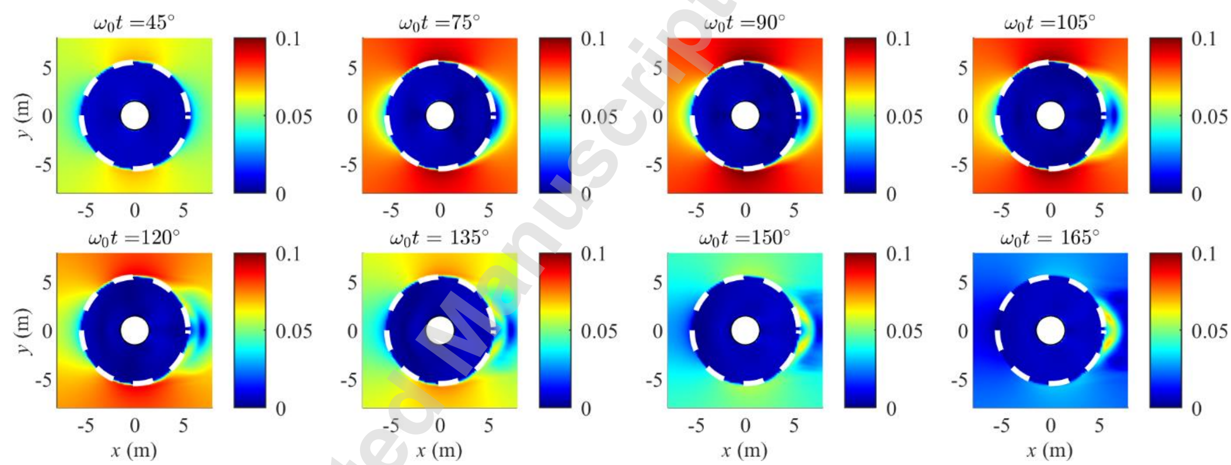

(a)

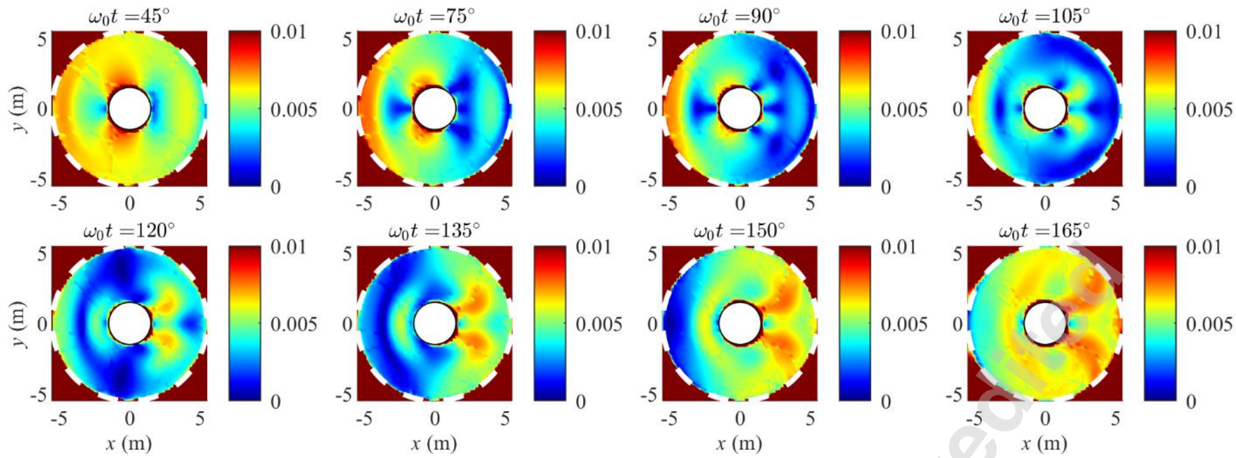

(b)

Fig. 22 Bed shear stress around the pile with scour protection at different phases for the crest half-period (U_m = 1.95 m/s, T = 12 s and KC_p = 7.8): (a) in the whole domain and (b) enlargement view inside the porous medium.

6. Conclusions

The present study investigates, using 2D and 3D numerical models, the flow around a mono-pile with scour protection. Both steady and oscillatory flow conditions are examined. In the model, the volume-averaged Reynolds-averaged Navier-Stokes (VARANS) equations are solved with the volume-averaged *k-ω* turbulence closure. The main conclusions are as follows:

(1) Near the interface between free flow and porous medium, the effect of porosity transition type on flow velocity, turbulence kinetic energy and bed shear stress is analysed, which is based on the experiments performed by Sumer et al. [1] and Stevanato et al. [31]. In comparison to the constant porosity and linear transition, the parabolic transition shows better agreement with the measurements.

(2) In the presence of monopile with scour protection, the model with parabolic transition considered is validated against the existing experiments [28]. The simulated flow patterns and turbulence levels are both consistent with the measurements, illustrating a good performance of the model. It is shown that the horseshoe vortex in the upstream of pile can penetrate into the scour protection, which induces high bed shear stress. As a result, the sediment particles are supposed to be transported upstream, causing the sinking of the protection layer.

(3) The model subsequently studies the oscillatory porous flow features around a pile. It is found that the horseshoe vortex and attached lee-wake vortices are formed at two sides of the pile, respectively. They penetrate into the entire scour protection layer, generating high flow velocities and bed shear stresses.

(4) In oscillatory flow, the horseshoe vortex in front of a pile emerges later than the lee-wake vortices near the porous medium. The lee-wake vortices first occur near the porous medium and gradually amplify to the free flow. At the right toe of the scour protection, an distinct local vortex rotating in a clockwise direction is also observed. The vortices all increase in both size and intensity with increasing phase in each half-period. The bed shear stress inside the scour protection is smaller compared to outside. Under the protection, it reaches the maximum at the side edges of the pile.

Journal of Offshore Mechanics and Arctic Engineering. Received February 21, 2022;
Accepted manuscript posted April 13, 2022. doi:10.1115/1.4054393

(5) The flow features under oscillatory condition are strongly influenced by KC_p. As the KC_p increases, the vortices inclusive of the horseshoe vortex and the lee-wake vortices, both in size and lifespan augments; the bed shear stress both inside and outside the scour protection also amplifies.

Acknowledgement

This work is carried out at the Mechanical Engineering Department of Denmark Technical University. The first author is supported by a three-year Ph.D. scholarship from the Chinese Scholarship Council (CSC).

References

[1] Sumer, B. M., Cokgor, S., Fredsøe, J., 2001. "Suction Removal of Sediment from between Armor Blocks," J. Hydraul. Eng., 127, pp. 293–306.

[2] Sumer, B.M., Fredsøe, J., Christiansen, N., 1992. "Scour Around Vertical Pile in Waves," J. Waterw. Port, Coastal, Ocean Eng., 118, pp. 15–31.

[3] Sumer, B.M., Fredsøe, J., 2002. "The Mechanics of Scour in the Marine Environments," World Scientific, Singapore.

[4] Breusers, H., Raudkivi, A., 1991. "Scouring. In: hydraulic structures design manual," Balkema, Rotterdam., 2.

[5] Hoffmans, G.J.C.M., Verheij, H.J., 2017. "Scour Manual," Routledge.

[6] Whitehouse, R.J.S., 1997. "Scour at marine structures: a manual for practical applications," Thomas Telford.

[7] Melville, B., Coleman, S.E., 2000. "Bridge scour," Water Resources Publications.

[8] Baykal, C., Sumer, B.M., Fuhrman, D.R., Jacobsen, N.G., Fredsøe, J., 2015. "Numerical investigation of flow and scour around a vertical circular cylinder," Philos. Trans. R. Soc. A Math. Phys. Eng. Sci., 373, 20140104.

[9] Harris, J.M., Whitehouse, R.J.S., Benson, T., 2010. "The time evolution of scour around offshore structures," Proc. Inst. Civ. Eng. - Marit. Eng., 163, pp. 3–17.

[10] Khosronejad, A., Kang, S., Sotiropoulos, F., 2012. "Experimental and computational investigation of local scour around bridge piers," Adv. Water Resour., 37, pp. 73–85.

[11] Kirkil, G., Constantinescu, S.G., Ettema, R., 2008. "Coherent Structures in the Flow Field around a Circular Cylinder with Scour Hole," J. Hydraul. Eng., 134, pp. 572–587.

[12] Liu, X., García, M.H., 2008. "Three-Dimensional Numerical Model with Free Water Surface and Mesh Deformation for Local Sediment Scour," J. Waterw. Port, Coastal, Ocean Eng., 134, pp. 203–217.

[13] Nielsen, A.W., Hansen, E.A., 2007. "Time-Varying Wave and Current-Induced Scour Around Offshore Wind Turbines," in: Volume 5: Ocean Space Utilization; Polar and Arctic Sciences and Technology; The Robert Dean Symposium on Coastal and Ocean Engineering; Special Symposium on Offshore Renewable Energy. ASMEDC, pp. 399–408.

[14] Sørensen, S.P.H, Ibsen, L.B., 2013. "Assessment of foundation design for offshore monopiles unprotected against scour," Ocean Eng., 63, pp. 17–25.

[15] Raaijmakers, T., Rudolph, D., 2008. "Time-dependent scour development under combined current and waves conditions - Laboratory experiments with online monitoring technique," Proc. 4th Int. Conf. Scour Erosion, ICSE,

Tokyo.

[16] Roulund, A., Sumer, B.M., Fredsøe, J., Michelsen, J., 2005. "Numerical and experimental investigation of flow and scour around a circular pile," J. Fluid Mech., 534, pp. 351–401.

[17] Zhao, M., Cheng, L., Zang, Z., 2010. "Experimental and numerical investigation of local scour around a submerged vertical circular cylinder in steady currents," Coast. Eng., 57, pp. 709–721.

[18] Hansen, E.A., Simonsen, H.J., Nielsen, A.W., Høgedal, M., Pedersen, J., 2007. "Scour protection around offshore wind turbine foundations, full-scale measurements," in: European Wind Energy Conference and Exhibition 2007, EWEC 2007.

[19] Nielsen, A.W., Sumer, B.M., Petersen, T.U., 2014. "Sinking of scour protections at Horns Rev 1 offshore wind farm," Coast. Eng. Proc., 1, 67.

[20] Petersen, T.U., Mutlu Sumer, B., Fredsøe, J., Raaijmakers, T.C., Schouten, J.-J., 2015. "Edge scour at scour protections around piles in the marine environment — Laboratory and field investigation," Coast. Eng., 106, pp. 42–72.

[21] Raaijmakers, T.C., van Oeveren, M.C., Rudolph, D., Leenders, V., Sinjou, W.C.P., 2010. "Field Performance of Scour Protection around Offshore Monopiles, in: Scour and Erosion," American Society of Civil Engineers, Reston, VA, pp. 428–339.

[22] Whitehouse, R.J.S., Harris, J.M., Sutherland, J., Rees, J., 2011. "The nature of scour development and scour protection at offshore windfarm foundations," Mar. Pollut. Bull. 62, pp. 73–88.

[23] Chiew, Y.M., 2002. "Failure mechanism of riprap layer around bridge piers," in: First International Conference on Scour of Foundations. College Station, USA, pp. 70–91.

[24] Lauchlan, C.S., Melville, B.W., 2001. "Riprap Protection at Bridge Piers," J. Hydraul. Eng., 127, pp. 412–418.

[25] Nielsen, A.W., Probst, T., Petersen, T.U., Sumer, B.M., 2015. "Sinking of armour layer around a vertical cylinder exposed to waves and current," Coast. Eng., 100, pp. 58–66.

[26] Sumer, B.M., Nielsen, A.W., 2013. "Sinking failure of scour protection at wind turbine foundation," Proc. Inst. Civ. Eng. – Energy., 166, pp. 170–188.

[27] Nielsen, A.W., 2011. "Scour Protection of Offshore Wind Farms," Ph.D. thesis, Technical University of Denmark, Denmark.

[28] Nielsen, A.W., Mutlu Sumer, B., Fredsøe, J., Christensen, E.D., 2011. "Sinking of armour layer around a cylinder exposed to a current," Proc. Inst. Civ. Eng. - Marit. Eng., 164, pp. 159–172.

[29] Dargahi, Bijan. 1989. "The turbulent flow field around a circular cylinder," Experiments in Fluids., 8 (1), pp. 1–12.

[30] Nielsen, A.W., Liu, X., Sumer, B.M., Fredsøe, J., 2013. "Flow and bed shear stresses in scour protections around a pile in a current," Coast. Eng., 72, pp. 20–38.

[31] Stevanato, F., Nielsen, A.W., Sumer, B.M., Fredsøe, J., 2010. "Flow Velocities and Bed Shear Stresses in a Stone Cover under an Oscillatory Flow," Scour and Erosion., pp. 609–618.

[32] Nielsen, Anders Wedel and Petersen, Thor Ugelvig. 2019. "Stability of cover stones around a vertical cylinder under the influence of waves and current." Coast. Eng., 154, 103563.

Journal of Offshore Mechanics and Arctic Engineering. Received February 21, 2022;
Accepted manuscript posted April 13, 2022. doi:10.1115/1.4054393

[33] Liu, P.L.-F., Lin, P., Chang, K.-A., Sakakiyama, T., 1999. "Numerical Modeling of Wave Interaction with Porous Structures," J. Waterw. Port, Coastal, Ocean Eng., 125(6), pp. 322–330.

[34] Troch, P., De Rouck, J., 1999. "An active wave generating-absorbing boundary condition for VOF type numerical model," Coast. Eng., 38, pp. 223–247.

[35] van Gent, M.R.A., 1995. "Porous Flow through Rubble-Mound Material," J. Waterw. Port, Coastal, Ocean Eng., 121(3), pp. 176–181.

[36] van Gent, M.R.A., 1995. "Wave Interaction with Permeable Coastal Structures," Ph.D. thesis, Delft University of Technology, Netherlands.

[37] Jensen, B., Jacobsen, N.G., Christensen, E.D., 2014. "Investigations on the porous media equations and resistance coefficients for coastal structures," Coast. Eng., 84, pp. 56–72.

[38] Losada, I.J., Lara, J.L., Losada, M.A., 2000. "Experimental study on the influence of bottom permeability on wave breaking and associated processes," Coast. Eng. 2000 - Proceedings of the 27th International Conference on Coastal Engineering, ICCE 2000.

[39] Sakakiyama, T., Liu, P.L.F., 2001. "Laboratory experiments for wave motions and turbulence flows in front of a breakwater," Coast. Eng., 44, pp. 117–139.

[40] Fang, H., Han, X., He, G., Dey, S., 2018. "Influence of permeable beds on hydraulically macro-rough flow," J. Fluid Mech., 847, pp. 552–590.

[41] Kuwata, Y., Suga, K., 2017. "Direct numerical simulation of turbulence over anisotropic porous media," J. Fluid Mech., 831, pp. 41–71.

[42] Liu, Q., Prosperetti, A., 2011. "Pressure-driven flow in a channel with porous walls," J. Fluid Mech., 679, pp. 77–100.

[43] Liu, Y., Stoesser, T., Fang, H., Papanicolaou, A., Tsakiris, A.G., 2017. "Turbulent flow over an array of boulders placed on a rough, permeable bed," Comput. Fluids., 158, pp. 120–132.

[44] Mandviwalla, X., Christensen, E.D., 2021. "Entrainment of sediment particles in protection layers," J. Hydraul. Eng., 147(10), 04021040.

[45] Mazzuoli, M., Uhlmann, M., 2017. "Direct numerical simulation of open-channel flow over a fully rough wall at moderate relative submergence," J. Fluid Mech., 824, pp. 722–765.

[46] Wilcox, D.C., 2006. "Turbulence Modeling for CFD (Third Edition)," DCW Ind.

[47] Nakayama, A., Kuwahara, F., 1999. "A Macroscopic Turbulence Model for Flow in a Porous Medium," J. Fluids Eng., 121, pp. 427–433.

[48] Sumer, B.M., 2007. "Mathematical modelling of scour: A review," J. Hydraul. Res., 45(6), pp. 723–735.

[49] Sumer, B.M., Fuhrman, D.R., 2020. "Turbulence in Coastal and Civil Engineering," World Scientific.

[50] Zhai, Y., Christensen, E.D., 2021. "Numerical simulations inside a stone protection layer with a modified k-ω turbulence model," Submitt. to Coast. Eng. Under Rev. March 2021.

[51] Sumer, B.Mutlu, Whitehouse, R.J.S., Tørum, A., 2001. "Scour around coastal structures: a summary of recent research," Coast. Eng., 44, pp. 153–190.

[52] Hsu, T.-J., Sakakiyama, T., Liu, P.L.F., 2002. "A numerical model for wave motions and turbulence flows in

Journal of Offshore Mechanics and Arctic Engineering. Received February 21, 2022;
Accepted manuscript posted April 13, 2022. doi:10.1115/1.4054393

front of a composite breakwater," Coast. Eng. 46, pp. 25–50.

[53] Fredsøe, J., Andersen, K.H., Mutlu Sumer, B., 1999. "Wave plus current over a ripple-covered bed," Coast. Eng., 38(4), pp. 177-221.

[54] Sumer, B.M., Arnskov, M.M., Christiansen, N., Jørgensen, F.E., 1993. "Two-component hot-film probe for measurements of wall shear stress," Exp. Fluids., 15, pp. 380–384.

[55] Schippers, M.M.A., Jacobsen, N.G., Dalyander, P.S., Nelson, T., McCall, R., 2017. "Incipient Motion of Sand-oil Agglomerates," Proceeding Coast. Dyn.

[56] Graf, W.H., Yulistiyanto, B., 1998. "Experiments on flow around a cylinder; The velocity and vorticity fields," J. Hydraul. Res., 36, pp. 637–654.

[57] Sumer, B.M., Chua, L.H.C., Cheng, N.-S., Fredsøe, J., 2003. "Influence of Turbulence on Bed Load Sediment Transport," J. Hydraul. Eng., 129, pp. 585–596.

[58] Sumer, B.M., Christiansen, N., Fredsøe, J., 1997. "The horseshoe vortex and vortex shedding around a vertical wall-mounted cylinder exposed to waves," J. Fluid Mech., 332, pp. 41–70.